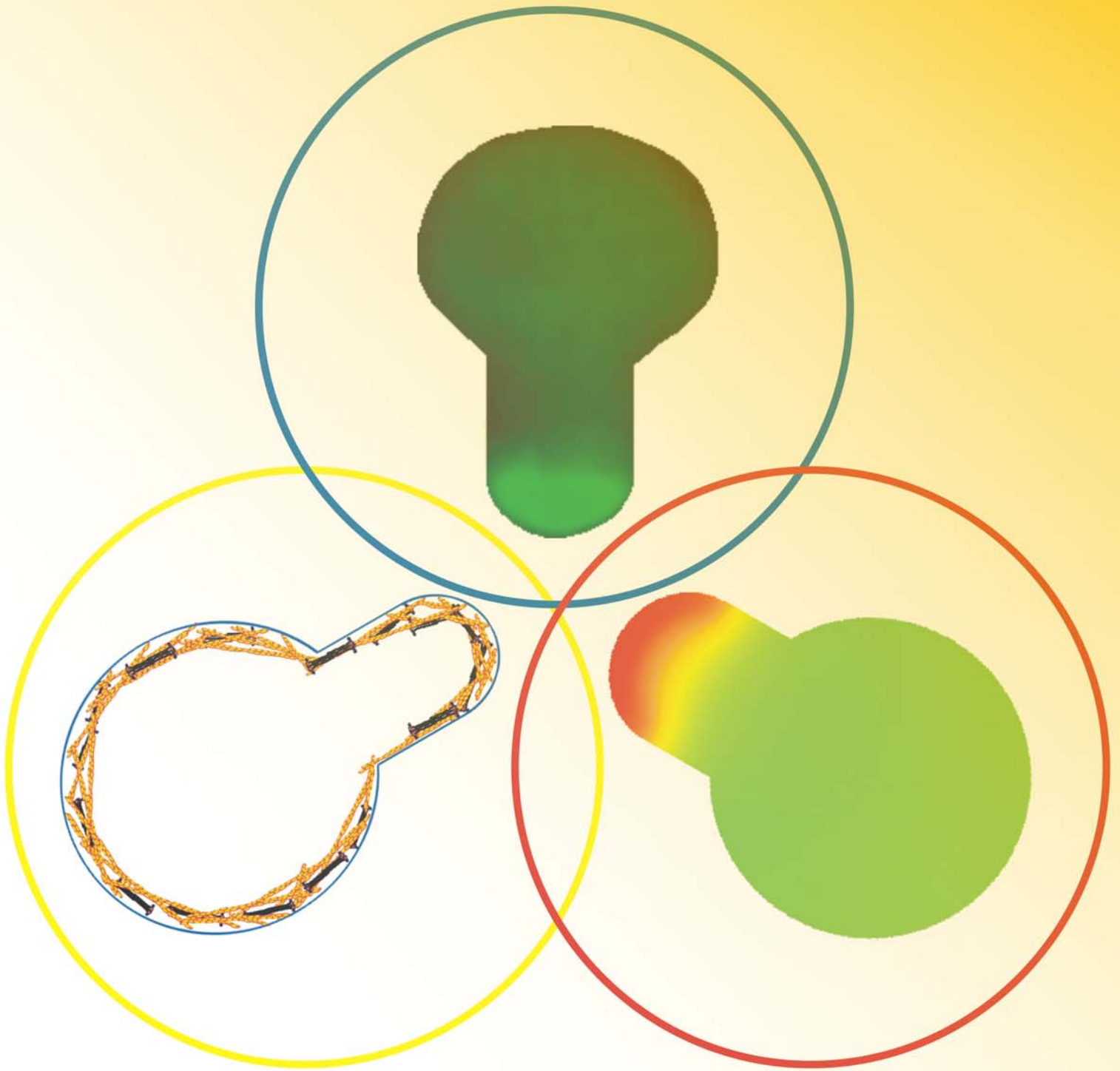# Biophysical
Journal

Understanding the cooperativity of myosin II from molecular level to cell level during mechanosensation--The trinity of experiments, theoretical models and numerical simulations.

Understanding the Cooperative Interaction between Myosin II and Actin Cross-Linkers Mediated by Actin Filaments during Mechanosensation

Tianzhi Luo,[†*] Krithika Mohan,[§] Vasudha Srivastava,[†¶] Yixin Ren,[†] Pablo A. Iglesias,[§] and Douglas N. Robinson[†‡¶*]

[†]Department of Cell Biology, [‡]Department of Pharmacology and Molecular Sciences, School of Medicine, [§]Department of Electrical and Computer Engineering, and [¶]Department of Chemical and Biomolecular Engineering, Whiting School of Engineering, The Johns Hopkins University, Baltimore, Maryland

ABSTRACT   Myosin II is a central mechanoenzyme in a wide range of cellular morphogenic processes. Its cellular localization is dependent not only on signal transduction pathways, but also on mechanical stress. We suggest that this stress-dependent distribution is the result of both the force-dependent binding to actin filaments and cooperative interactions between bound myosin heads. By assuming that the binding of myosin heads induces and/or stabilizes local conformational changes in the actin filaments that enhances myosin II binding locally, we successfully simulate the cooperative binding of myosin to actin observed experimentally. In addition, we can interpret the cooperative interactions between myosin and actin cross-linking proteins observed in cellular mechanosensation, provided that a similar mechanism operates among different proteins. Finally, we present a model that couples cooperative interactions to the assembly dynamics of myosin bipolar thick filaments and that accounts for the transient behaviors of the myosin II accumulation during mechanosensation. This mechanism is likely to be general for a range of myosin II-dependent cellular mechanosensory processes.

INTRODUCTION

Nonmuscle myosin II is critical for many cellular events, such as motility, cell division, and tissue morphogenesis. In the past few decades, much effort has been invested to understand its roles in mechanosensation and mechanotransduction at the single molecule, cellular, and tissue levels (1–4). Yet, the mechanisms of its cellular functions and its interactions with other proteins remain to be clarified. One of the interesting findings is the cooperative binding of myosin heads to actin filaments (5–7). Under specific conditions in vitro, the level of actin-bound myosins displayed a sigmoidal increase as a function of increasing myosin concentration and clustering along the actin filaments. These observations suggest cooperative interactions between myosins (homocooperativity). In *Dictyostelium,* myosin II and the actin cross-linker cortexillin I also codependently accumulate into the highly deformed regions induced by micropipette aspiration (MPA) (2). Furthermore, the extent of myosin II accumulation increases monotonically with increasing applied force in a manner that is dependent on its lever-arm length (3). Although the latter can be qualitatively interpreted by the force-dependent binding affinity to actin filaments (8) and the lever-arm theory of myosin (9), the underlying mechanism of the heterocooperativity between these two different proteins remains elusive.

In the absence of regulatory proteins (such as troponin and tropomyosin), the mechanism for myosin homocooperativity was suggested to occur because binding of myosin

heads causes local conformational changes in actin subdomain 2, facilitating myosin binding nearby (7). Other proteins, such as cofilin, espin, and fascin, also display cooperative binding to actin filaments due to the conformational changes in actin upon binding (10–13). Importantly, actin filaments had increased torsion and bending flexibility due to cofilin binding and twisting due to espin and fascin binding. Based on these observations, the conformational changes of actin due to protein binding may be essential for cooperative binding of proteins to actin filaments although the details of the atomic level deformations are still absent.

Though myosin II biochemical and biophysical assays have revealed the underlying mechanisms of cooperativity, there are several missing links between these in vitro observations and the cellular behaviors: First, most mathematical descriptions of cooperativity were based on fitting the experimental data to the general Michaelis-Menten equation or Hill equation (5,6), which by itself does not reflect the molecular scale mechanisms of the process. Second, most studies only considered the cooperative interaction between nearest neighbors, thereby ignoring the propagation of actin monomer deformations over longer distances and significantly underestimating cooperativity (14). Third, because the basic functional unit of myosin II is the bipolar thick filament (BTF), a mathematical model that links the force-dependent myosin-actin interactions, myosin cooperativity and the BTF assembly kinetics is required. Specifically, because actin filaments significantly enhance the BTF assembly rate and the myosin-actin binding is force-dependent, these features must be considered in the model (8,15). However, the current understanding of myosin

cooperativity is based either on measurements of the myosin motor (proteolytic subfragment 1, S1) or the dimerized motor (heavy meromyosin) to actin filaments in the absence of applied force (5–7). The fourth issue is that in vivo protein concentrations are more spatially heterogeneous than those in the in vitro assays (16,17). Differences also exist in the mechanical studies of in vitro assembled actin networks where the imposed deformations are relatively uniform. However, the deformations experienced by cells, such as through atomic force microscopy or MPA, are typically much more localized, leading to deformation gradients (18), which are likely to be more physiologically relevant for normal cell behaviors. Therefore, for a quantitative interpretation of the in vivo cell behaviors based on the understanding of in vitro assays, a multiscale model that integrates these factors is required.

In this article, we analyzed the heterocooperativity between myosin II and cortexillin I in *Dictyostelium* cells. We then reproduced the key features of the experimental observations of both homocooperativity and heterocooperativity using simulations. These simulations were based on one essential assumption: myosin binding to actin causes local conformational changes in the actin that enhance myosin binding in nearby regions. We performed two-dimensional coarse-grained kinetic Monte Carlo simulations of homocooperativity of myosin head binding. The simulations yielded the sigmoidal curve and the two-dimensional cluster formation observed in biochemical assays. Moreover, we simulated the mixed system containing myosin and cortexillin, assuming that myosin binding alone promotes further myosin and cortexillin binding. In these simulations, cortexillin binding always followed myosin binding kinetically and the two-dimensional clusters contained mixtures of both proteins. Furthermore, we developed a model for myosin bipolar thick filament (BTF) assembly by incorporating the effect of myosin head binding through mean-field approximation into the BTF dimer addition model. This model accounts for the kinetics and three-dimensional pattern of the cooperative accumulation of myosin observed experimentally during MPA.

MATERIALS AND METHODS

Measurements of mechanosensory response of proteins using MPA

Micropipette aspiration was performed as described previously (2). In short, to apply aspiration pressure, the pressure difference was generated by adjusting the height of a motor-driven water manometer. The *Dictyostelium myosin II* null cells (cells deleted for the *myosin II heavy chain* gene, *mhcA*) were transformed with GFP myosin II (GFP-mhcA) and mCherry cortexillin I plasmids or GFP 3×Ala myosin II (a mutant myosin II heavy chain where key threonines, which are phosphorylated by heavy chain kinases, are mutated to alanine). WT cells were transformed with the GFP myosin heavy chain kinase C (GFP-MHCK-C) plasmid (19).

Cells were loaded into the observation chamber filled with sterile filtered MES buffer (50 mM MES at pH 6.5, 2 mM MgCl$_2$, 0.2 mM CaCl$_2$).

Latrunculin-A and jasplakinolide were used to change the F-actin level in cells as compared to DMSO-carrier treated controls (see the Supporting Material). The images were collected using an IX81 microscope (Olympus, Melville, NY) and analyzed using ImageJ software (National Institutes of Health, Bethesda, MD). After background correction, the fluorescence intensity at the accumulation site inside the micropipette was normalized against the opposite cortex in each frame to account for photobleaching. The fluorescence signals were assumed to be linearly proportional to the concentrations of the corresponding protein.

Two-dimensional coarse-grained kinetic Monte Carlo model

To study the kinetics of cooperative binding, a coarse-grained kinetic Monte Carlo simulation model is introduced. A similar model has proven to be powerful for predicting the kinetics of reaction-diffusion systems (20). The simulation domain is a two-dimensional matrix of $N \times N$ square lattices (see Fig. S1 in the Supporting Material). Actin monomers are 5.4 nm in diameter and F-actin filaments are composed of two intertwined strands that are staggered by half a monomer, i.e., 2.7 nm. Because each myosin head covers two actin monomers along a single strand, each lattice point has a size of $a = 5$ nm, representing one myosin binding site along the actin filament. Two actin filaments are orthogonally aligned at $x = N/2$ and $y = N/2$ to mimic the actin network. The simulated mesh size of the actin network is Na. Two-dimensional periodic conditions are applied to the diffusion process but diffusion of bound myosins on F-actin is not allowed. It is assumed that myosin heads have two energy states: unbound and bound state (neglecting the details of the bound myosins with different nucleotide states). The strain energy associated with myosin binding is E_s^0 and decays exponentially along the actin filament (shown in Fig. S1 *B*), i.e.,

$$E_s^j(x_{ij}) = E_s^0 \exp\left(-\frac{|x_{ij}|}{\lambda}\right),$$

where $|x_{ij}|$ is the distance between binding sites i and j (21). The characteristic decay length, λ, was set to $2a$ because it was observed experimentally that the deformation associated with the binding of a single myosin head propagates ~3–4 actin monomers along a single strand (14). The binding energy of a myosin head, which depends on the occupation states of its neighboring binding sites, is

$$E_i = E_i^0 + \sum_j E_s^j(x_{ij}),$$

where E_i^0 is the binding energy in the absence of strain. To speed up the computation, a lookup table was used for $|x_{ij}| \leq 3a$, containing 30 different cases in terms of occupation state of 2×3 neighboring binding sites. The energy error at a cutoff of $3a$ is ~0.14 E_s^0. If $|x_{ij}| \leq 4a$ is used, the corresponding energy error decreases to 0.08 E_s^0 but the lookup table includes 56 different cases complicating the computations.

Here, the rates of diffusion and binding are kept constant and only the unbinding rate is allowed to be affected by the strain energy associated with cooperative binding through the form of binding energy as defined above. Namely, the energy level of the transition state is assumed to be unaffected by the cooperative binding (see Fig. S1 *C*). The reasoning behind this assumption is that the ADP-bound isometric state of myosin (where a myosin head tightly binds actin) is the critical state for myosin cooperative binding (22). The energy landscape is shifted from solid line to dotted line upon the cooperative binding (see Fig. S1 *C*). The unbinding rate has the form $k_{off} = v \exp(-E/k_BT)$, where E is the associated energy barrier, k_B is the Boltzmann constant, T is the temperature, and v is the vibration frequency at the molecular level. This energy barrier, $E = E_a + E_i$, where E_a is the activation energy barrier, is assumed not to change with

cooperative binding. There is no reported value for E_a as it is difficult to measure experimentally. To overcome this issue, the rate equation is rewritten as

$$k_{off} = k_{off}^0 \exp\left(-\sum_j E_s^j \frac{(x_{ij})}{k_B T}\right),$$

where k_{off}^0 is the unbinding rate of single myosin head in the absence of cooperativity and has a reported value ~300.0 s^{-1} (23). The value k_{off}^0 alone contains information of the energies E_a and E_i^0. Thus, without knowing the exact values of E_a and E_i^0, the effect of cooperative binding on k_{off} may be evaluated by adjusting E_s^0 because E_s^j depends on E_s^0. The binding rate is set to 10.0 s^{-1}, corresponding to the period of myosin ATP hydrolysis cycle (100 ms, (23)). The kinetic rate for diffusion events is chosen to be 3.0×10^7 s^{-1} corresponding to a three-dimensional diffusion coefficient of ~0.2 μm^2/s (24). Although a myosin II monomer has two heads, whether the myosin heads belong to different monomers or the same does not affect their binding behaviors in simulations.

Myosin thick filament assembly in the presence of actin filaments

Previously, we proposed a detailed dimer addition scheme for BTF assembly/disassembly based on in vivo and in vitro observations (3,25,26). In this case, the BTF is formed through dimer addition and the stacking of the tail domain of each monomer. The diameter of the *Dictyostelium* myosin BTFs increases but their length does not change as the BTFs grow, which is different from the muscle myosin BTF assembly mechanism. The BTF assembly scheme primarily consists of five steps, each described by forward, k_i, and backward, k_{-i}, rates ($i = 1, 2, ..., 5$), respectively. The values k_2, k_3, k_4, and k_{-5} are based on experimentally measured values (25,27,28). Other rates are determined numerically by fitting the experimental observation that 20% of myosins are assembled into BTFs (25,27).

Importantly, numerical tests suggest that the ratio of the rates describing the conversion between incompetent and competent states is the most sensitive parameter that controls the assembly dynamics and therefore, is the only one that is likely to have strain-dependence (3). However, the effect of the cooperative binding of myosin heads in the presence of actin filaments was not considered previously. Myosin binding to actin has at least two effects on BTF assembly: First, the binding is required for myosins to sense the tension in actin filaments. Second, binding prevents myosin monomers from diffusing away from the actin filaments, increasing the probability of the tail-domain interactions between neighboring bound monomers, which elevates BTF assembly.

Here, we incorporated the effect of actin filaments into the kinetics of myosin BTF assembly and present an updated scheme. Due to the presence of actin, the myosin monomer has four different forms: competent bound; incompetent bound; competent unbound; and incompetent unbound. These myosin forms are denoted by M^*, $\overline{M}^*$, M and $\overline{M}$, respectively, where the overbar represents "incompetent" and the asterisk represents "bound". The change between competent and incompetent states is a structural one and is presumed to be uncoupled from the change between bound and unbound states.

This updated framework takes into account the conversion between the four different myosin monomer forms and the cooperative binding effect, and is shown in Fig. 1. It is thought that the conversions between incompetent and competent states are governed by MHCK and phosphatase in cells (27). Thus, k_+ is set to be 0.05 s^{-1} based on the measured myosin tail dephosphorylation rate (29). However, no experimental data on the phosphorylation rate are available. Therefore, k_- needs to be set numerically. The value k_1, the rate that controls the conversion from the bound and the unbound states, has the form of $k_1 = k_{on}C_{actin}$, where k_{on} is the on-rate for myosin binding to actin and is ~0.45 μM^{-1} s^{-1} (30). Because
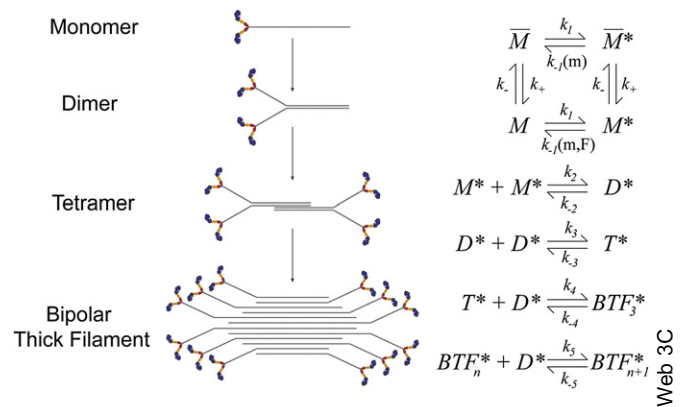

FIGURE 1 Dimer addition model for myosin BTF assembly in the presence of actin filaments. M, D, and T represent the monomer (the hexameric monomer with two heavy chains, two essential light chains, and two regulatory light chains), dimer, and tetramer, respectively, BTF$_3$, BTF$_n$, and BTF$_{n+1}$ are the bipolar filaments having 6, $2n$, and $2(n+1)$ monomers, respectively, and n is the number of dimers. The superscripts (*) and bar ($-$) represent the actin-bound state and the incompetent forms, respectively. The rate constant $k_1 = k_{on}C_{actin}$, where k_{on} is the on-rate for myosin binding to actin and C_{actin} is the F-actin concentration; k_- can be determined by the BTF concentration at steady state. The value k_{-1} is a function of the concentration of myosin (m) and/or applied force (m, F).

myosin unbinding to actin is force-dependent (8) and the isometric binding state is crucial for cooperativity (22), it is reasonable to incorporate its associated cooperative effect in the rate k_{-1} that controls the conversion from the bound and the unbound states.

Considering the abundance of actin filaments in cells and that the assembly rate of BTFs in the presence of actin filaments is much higher than that of myosin alone (15,28), we suspect that although BTFs can still form without binding to actin, the turnover dynamics of myosin BTFs is dominated by the scheme associated with myosin binding to actin. The primary unit for the BTF assembly described is the competent bound myosin M^*. Anything that promotes the conversion from $\overline{M}^*$ or M to M^* accelerates BTF assembly. So far no experimental evidence indicates that the conversion from $\overline{M}^*$ to M^* (i.e., the dephosphorylation of myosin tail) is force-dependent. However, accumulating evidence, including the simulations presented here, points to the force-dependency of the conversion from M to M^* (8). Therefore, k_{-1} is the key parameter that controls the force-induced myosin accumulation and subsequent BTF assembly. Based on the mean-field approximation of homocooperativity of myosin, k_{-1} has the form of

$$k_{-1} = k_{-1}^0 \exp\left(-\frac{\Delta E_b}{k_B T}\right), \tag{1}$$

where k_{-1}^0 is the rate in the absence of force and homocooperativity, and ΔE_b is the change of binding energy of a myosin head to actin due to the applied force and the cooperative binding. The measured value of k_{-1}^0 is ~300.0 s^{-1} (23). In general, ΔE_b can be described as

$$\Delta E_b = E_s + fd + \Phi(E_s, f), \tag{2}$$

where f is the force applied on each myosin head and the force-dependent bond length d is an empirical parameter that can be obtained by single molecule measurements according to Bell's model. Each myosin head is able to generate ~4 pN of force to counteract the external load. The value d is in the range of 1–2 nm (31). The value Φ is the additional strain energy, a coupling term of E_s and fd when neighboring bound myosins are deformed by the force f. A simple choice is $\Phi \sim fdE_s$. Experimental data

suggest that the increase of binding energy due to tension may be related to the prolonged transition state of the actin-bound myosin before phosphate release (7,15,22). $f \sim m^{-1}$ because the total force is shared by all bound myosins, i.e., $F \sim mf$, where F is the total force and m is the total number of bound myosins. As described in the results (below), E_s is approximately a piecewise linear function of the coverage of the actin filament by myosin, implying $E_s \sim m$. Based on the above scaling analysis, the coupling term Φ is independent of m but proportional to the applied force F and the force-independent strain energy E_s^0, i.e., $\Phi \sim FdE_s^0$. As a result, Eq. 1 can be rewritten as

$$k_{-1} = k_{-1}^0 \exp\left(-\frac{\left(\Delta E_b' + \omega FdE_s^0\right)}{k_B T}\right), \qquad (3)$$

where $\Delta E_b'$ contains the terms dependent on the amount of bound myosin m, and ω is a coefficient characterizing the energy coupling. The coupling term is for the completeness of the formulation and it can be neglected for convenience because it is a higher order term. Therefore, we used $k_{-1} = k_{-1}^0 \exp(-\Delta E_b'/K_B T)$ in all simulations.

RESULTS

Myosin and cortexillin show cooperative accumulation during micropipette aspiration

We used MPA to apply aspiration pressure to cells and observed the concentration changes of myosin and cortexillin at the deformation site (Fig. 2 A). The local concentrations of myosin and cortexillin typically increased in the aspirated region simultaneously with continuously increasing slopes in the rising phase. Importantly, both the peak intensity and the accumulation rate of myosin in the rising phase increased with applied pressure (Fig. 2, B and C). Because the initial myosin concentration in the cell cortex is ~4 μM and the local myosin concentration increased as much as threefold, this suggests that the accumulation rate can be up to 0.2 μM/s. We found that actin monomers and the actin binding proteins that bind to newly formed actin filaments, such as dynacortin, coronin, and LimE, did not show any concentration change in the tip region during MPA (data not shown, and Effler et al. (2)).

Furthermore, latrunculin-A treatment reduced the total actin and dramatically increased cell deformability, making it impossible to apply enough pressure to induce myosin mechanosensitive accumulation (see Fig. S2). On the other hand, increasing the total actin concentration fourfold using the actin stabilizer jasplakinolide did not alter the myosin stress-induced accumulation (see Fig. S2). All of these results, in combination, suggest that myosin mechanosensitive accumulation does not simply result from changes in the local F-actin concentrations. Because the mechanical input (external pressure) is constant for each curve, a positive feedback loop likely accelerates myosin accumulation by acting primarily at the level of the myosin-actin interaction. Cooperative binding of myosin to actin is one of the possible mechanisms to account for this loop.

We propose that myosin II mechanosensitive accumulation is caused by the force-induced bias of myosin binding
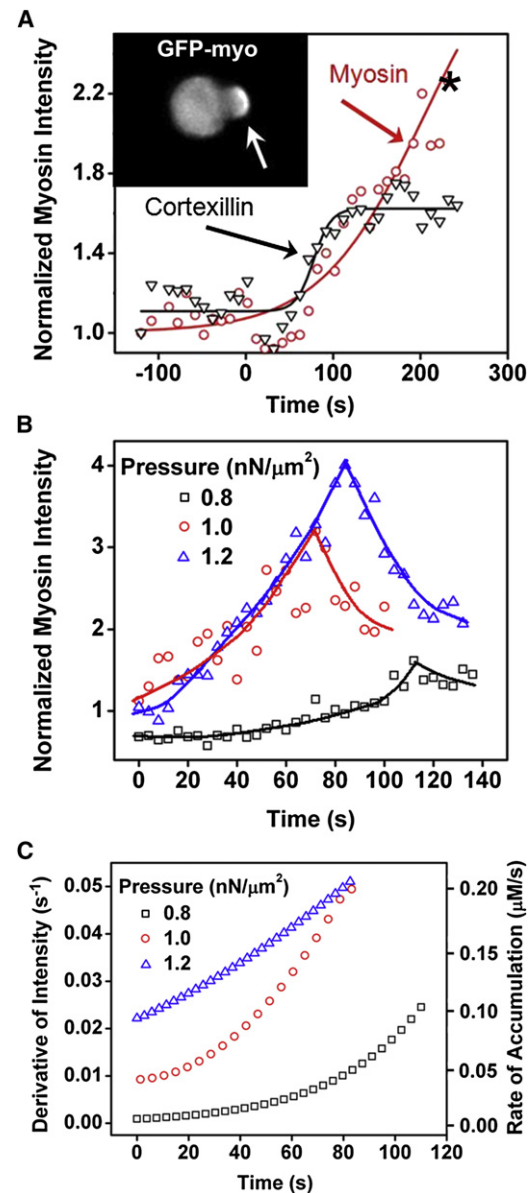

FIGURE 2   Mechanosensitive accumulation of myosin II and cortexillin I. (A) The transient curves of the accumulation of myosin II and cortexillin I of a single wild-type cell. (Asterisk in the graph) Point where the inset was derived. (Inset) Spatial pattern of GFP-myosin II accumulation during mechanosensing. (Open arrow) Tip position inside the micropipette. (B) The normalized myosin II accumulation magnitude increases overtime at different pressures. (Scattered symbols) Experimental data and lines show the trend. (C) The corresponding accumulation rates calculated from the data in panel B with initial cortical myosin concentration of 4.2 μM (17).

affinity to actin filaments, which enhances the myosin binding in the deformed regions. The basic functional unit of myosin is the myosin BTF, as the unassembled myosin monomer is unable to generate force. The majority of the accumulated myosin comes in monomer form from other regions by diffusion. The basis of this assumption is that a mutant myosin II heavy chain (3×Ala myosin II), which constitutively assembles into BTFs, has attenuated

mechanosensitive accumulation (3). To fully understand the kinetics of protein accumulation, it is necessary to consider both myosin binding to actin and the turnover dynamics of myosin BTFs. We will discuss them sequentially below and present a model that is able to explain the in vitro cooperative binding and the enhanced myosin BTF assembly in the presence of actin filaments (7,15,22), as well as the myosin accumulation observed during cellular mechanosensation.

Strain-induced cooperative interaction of myosin heads leads to cluster formation along actin filaments

We studied the homocooperativity of myosin II and the heterocooperativity between myosin II and cortexillin I using a two-dimensional coarse-grained kinetic Monte Carlo simulation model (see Materials and Methods). In this model, an actin meshwork was mimicked by a two-dimensional periodic rectangular box in which two actin filaments were orthogonally placed. Myosin and cortexillin proteins in the domain are allowed to diffuse, bind, and unbind the actin. Because the kinetic rates and geometries are based on three-dimensional considerations, the two-dimensional simulations reasonably mimic the kinetics of three-dimensional events (see the Supporting Material).

The bound fraction of myosin as a function of the myosin head concentration shows a sigmoidal shape, a signature of cooperativity (Fig. 3 A). It becomes more pronounced as the strain energy, E_s^0, increases, indicating that the cooperativity is proportional to the conformational change due to myosin binding. The cooperativity can be significant even when strain energy is only a few $k_B T$, a small portion of the ATP hydrolysis energy (~25 $k_B T$). Fitting the kinetics of binding to an exponential function suggests that the characteristic time of the curves is around a few seconds, consistent with published values (6). The two-dimensional myosin II clusters on actin due to homocooperativity (Fig. 3 B, and see Movie S1 in the Supporting Material) are similar to those observed previously by electron microscopy (7). Moreover, the cluster size increases with the strain energy due to cooperative binding (Fig. 3 C). In comparison, if we only consider nearest-neighbor interactions, the impact of cooperativity is much less, and the strain energy needs to be increased by up to eightfold to achieve similar cluster sizes (see Fig. S3). Thus, the above simulations replicate two major features observed in the in vitro myosin binding assays: the sigmoidal shape of myosin binding and the myosin clusters, suggesting that the simulation scheme and the parameters being used have physical and biological significance.

In cells, myosin heads undergo a power stroke, pulling the actin filaments along one direction. This myosin force-generation leads to an almost equivalent tension in the actin filaments if the polymers are cross-linked and/or entangled. Single molecule studies demonstrated that the tension is
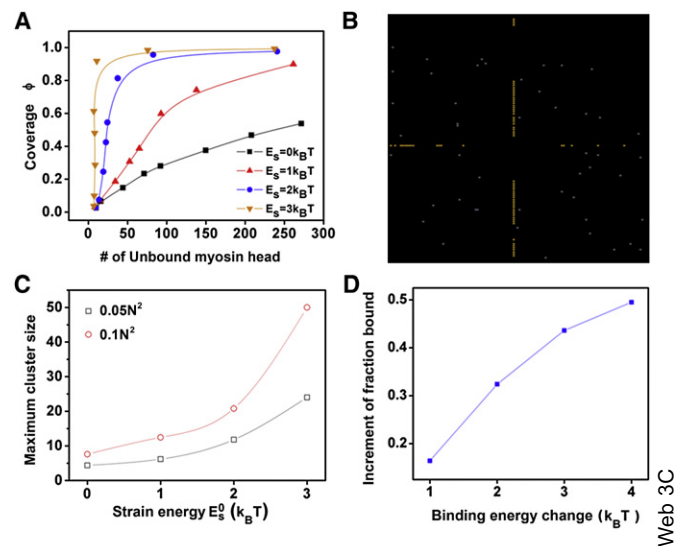

FIGURE 3 Simulation results of homocooperative binding of myosin II to the actin filaments. (A) Coverage of actin filaments by bound myosins, ϕ (i.e., the fraction of myosin binding sites on actin occupied by myosin) as a function of initial myosin concentrations at different strain energies. (B) A representative snapshot of myosin clusters (*aligned bright dots*) on the actin filaments. (*Scattered shaded dots*) Freely diffusing monomers. (C) The cluster size increases with E_s^0 in the cases where the total number of myosin is either 0.05 N^2 (*open squares*) or 0.1 N^2 (*open circles*). (D) The fraction of bound myosin increases with increasing strain energy, E_s^0. The simulation window size was $N = 128$.

able to lock the myosin heads in the isometric state and hence increase its binding lifetime to actin filaments (8). The relation between the tension and the binding lifetime is often described by Bell's model, i.e., the binding lifetime is exponentially proportional to the force experienced by each myosin head. During MPA experiments, the elevated pressure increases the tension in the actin filaments and consequently myosin heads experience more load, presumably leading to more local strain associated with myosin binding, as well as longer binding lifetimes. In simulations, the strain energy was increased with different magnitudes to mimic the effect of pressure jumps in experiments (Fig. 3 D). The bound fraction increases as the strain energy increases, consistent with the experimental observation that myosin accumulation increases as a function of applied pressure (Fig. 2 and Ren et al. (3)).

Because myosin and cortexillin synchronously accumulate during the rising phase (Fig. 2 A), we suggest that heterocooperativity may exist between myosin and cortexillin. To account for this, we consider that similar to myosin, cortexillin may have two energy states and that cortexillin's binding energy in the absence of strain (E_i^0) is similar to that of myosin's (experimental measurement of cortexillin's binding energy states are not yet available). Cortexillin binding to actin may also be cooperative. However, the binding lifetime of cortexillin to actin displayed no force-dependency over a 2.0 pN range in single molecule experiments, and *myosin II* null cells did not show mechanosensitive

GFP-cortexillin accumulation during MPA (3). These observations suggest that the cooperativity from cortexillin binding alone is not sufficient to mediate mechanosensitive cortexillin accumulation.

Therefore, we consider two extreme cases. The first is that the cooperativity of cortexillin binding is as strong as that of myosin binding and that the associated conformational change of actin facilitates both myosin and cortexillin binding. The second is that cortexillin binding is not cooperative. In both cases, it is assumed that myosin binding promotes cortexillin binding. For the first situation, cortexillin is not distinguishable from myosin based on their binding behaviors and the corresponding simulation result is not different from the case of pure myosin (not shown). For the second situation, the simulation shows that the dynamics of the protein binding of the mixed system is dominated by myosin and the corresponding clusters have both proteins (Fig. 4, and see Movie S2 and Fig. S4). Cortexillin accumulates as myosin does in both cases, suggesting that it will also accumulate in cases between the two extremes. Therefore, it is reasonable to conclude that heterocooperativity may be observed as long as myosin binding enhances cortexillin binding, whereas cortexillin binding does not need to enhance myosin binding.

With the essential assumption that local deformation of actin filaments due to myosin binding enhances neighboring myosin binding, these simulations qualitatively reproduce key features observed in the in vitro myosin binding assays and account for the possible heterocooperativity observed in vivo. Without this assumption (i.e., E_s^0 is zero), the sigmoidal curves and cluster formation disappeared (not shown).

Mean-field approximation of strain energy from statistical mechanics

To link quantitatively the cooperative interaction of myosins to the accelerated myosin accumulation observed in exper-

iments, we need to evaluate the average change of the binding energy E_s associated with the cooperative binding, as a function of the coverage of actin filaments by myosin binding, ϕ. An analytical solution for E_s might generally be obtained for simple cooperative interactions between proteins by considering nearest-neighbor interactions (32). However, the situation here is more complicated. Initially, myosin heads bind to actin filaments more-or-less randomly and slowly form clusters due to the cooperative interactions through the strain field in the actin filaments (see Movie S1). In addition to the inherent randomness of the occupied states of neighboring binding sites (more than just nearest-neighbor binding sites), the long-range nature of this type of cooperative interaction makes it almost impossible to obtain an analytical equation to calculate the average change of the binding energy. However, the average effect may be evaluated through statistical simulations.

To this end, we considered a one-dimensional actin filament with N binding sites for myosin and applied a periodic boundary to it to mimic an infinitely long filament. Using only the values of E_s^0 and the decay length of the strain field (λ), the mean-field approximation of the change of binding energy due to cooperative binding, E_s, can be calculated (see the Supporting Material) from

$$E_s(N, \phi) = \sum_{i=1}^{N\phi} \sum_{k=0}^{3} E_s^0 \exp\left(-\frac{|x_{ik}|}{\lambda}\right). \qquad (4)$$

Here, we assumed that E_s^0 can be as large as 3 $k_B T$. This assumption is derived from the precedent that the free energy change associated with cooperative actin binding of another actin binding protein, cofilin, is ~7 kJ/mol (~2.8 $k_B T$) (33). The value λ has the same value used previously (2a). We calculated E_s as a function of ϕ for different N and E_s^0 (Fig. S5, A–C). From this calculation, we find that regardless of the value of N, E_s can be approximated by a piecewise linear function as

$$E_s = \begin{cases} \chi_1 \phi, & \phi \leq \phi^* \\ \chi_1 \phi^* + \chi_2(\phi - \phi^*), & \phi > \phi^*, \end{cases} \qquad (5)$$

where χ_1 and χ_2 are the slopes and ϕ^* is the critical point where E_s switches between these two regimes. Because $\chi_1 > \chi_2$, E_s increases less after ϕ exceeds ϕ^* for $E_s^0 = 1, 2$, and 3 $k_B T$. Notably, χ_1, χ_2, and ϕ^* are dependent on E_s^0. For any $E_s^0 < 3$ $k_B T$, the corresponding triplet (χ_1, χ_2, ϕ^*) can be obtained simply by interpolation on the curves shown in Fig. S5 D.

The value of instantaneous E_s can be calculated through Eq. 5 once the concentrations of bound myosin and F-actin are known. The result of the mean-field approximation of E_s will be used in a myosin BTF assembly scheme described in the next section to evaluate the myosin accumulation.
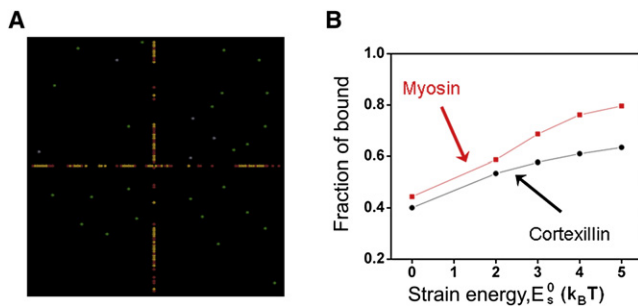

FIGURE 4   Simulation results of heterocooperative binding of myosin II and cortexillin I to the actin filaments. (A) A representative snapshot of the clusters formed by myosin and cortexillin due to heterocooperativity. (Yellow and red dots) Bound myosins and cortexillins, respectively; (gray and green dots) unbound myosins and cortexillins, respectively. (B) The fraction of bound proteins at steady state increases as a function of strain energy, E_s^0.

A model of myosin BTF assembly demonstrates strain-induced myosin accumulation

We developed a myosin BTF assembly model that takes into account the cooperative interaction and force-dependency of myosin binding to actin filaments (Materials and Methods, Fig. 1). The effect of cooperative interaction and force-dependency is reflected in the rate, k_{-1}, that controls the conversion from the bound to the unbound states through Eq. 3. Based on the scaling discussion, $\Delta E'_b$ in Eq. 3 has the form $\Delta E'_b = \delta m + Fd/\alpha m$, where the first term represents the strain energy and the second term is associated with the applied force with the coefficients α and δ. Specifically, αm is the amount of the bound BTF (the functional unit able to generate contractile force), and $\delta = 3\chi/C_{actin}$, where χ is the slope derived in the mean-field approximation (see previous section) and C_{actin} is the F-actin concentration. The terms m and ϕ are related by $\phi = 3m/C_{actin}$ where the factor 3 comes from the assumption that each binding site consists of three neighboring actin monomers in a double-helical actin filament (15). The piecewise linear approximation of E_s from the mean-field approximation may now be rewritten as

$$E_s = \begin{cases} \delta_1 m, & m \leq m^* \\ \delta_1 m^* + \delta_2(m - m^*), & m > m^*, \end{cases} \quad (6)$$

where m^* corresponds to ϕ^* in Eq. 5, δ_1 and δ_2 are the slopes, and $\delta_1 > \delta_2$. Indeed, δ_1 and δ_2 are related to χ_1 and χ_2 by a factor $3/C_{actin}$, respectively. Therefore, δ can have a value of either δ_1 or δ_2 depending on the amount of bound myosin m. The dependence of $\Delta E'_b$ on m for different E_s^0 is discussed in the Supporting Material.

The only undetermined rate in the scheme, k_-, was determined numerically by fitting the simulation results to the experimental observation that the immobile fraction of myosin in the cortex is between 20 and 50% because the immobile fraction measured by FRAP is equivalent to the assembled BTF fraction (34).

We applied the BTF assembly scheme with Eqs. 3 and 6 to different cases and compared the simulation results to the experimental observations. We also performed sensitivity tests of k_- and k_+ terms, which are provided in the Supporting Material.

Here, we present the simulation results of myosin accumulation in response to pressure. In *Dictyostelium* cells, C_{actin} is ~70 μM, which sets k_1 to be ~30.0 s^{-1}. In MPA measurements, the aspiration pressure ΔP was fixed over time and hence the total force F applied on the tip of cell in the pipette was constant. Initially, the system resides at steady state before time zero and then starts to evolve in response to the applied force, Fd. In the simulations, the concentration of unbound myosin monomer was kept constant (see the Supporting Material) and the value of Fd was varied over a physiological range (see Materials and Methods) to mimic different applied pressures. The kinetics

of BTF assembly along with the normalized myosin accumulation and the rates of accumulation with k_1 at 7 and 14 s^{-1} are provided (see Fig. S9). Importantly, the BTF assembly rate was nearly identical to the accumulation rates under the same conditions. With $k_1 = 7$ s^{-1}, BTF assembly increased, leading to significant myosin accumulation in response to applied force. However, these simulations did not show continuously increasing accumulation rates over the duration of force application. In comparison, with $k_1 = 14$ s^{-1}, the simulations showed dramatic BTF assembly and myosin accumulation and, most importantly, continuously rising accumulation rates even with smaller Fd. Quantitatively, the accumulation rate in the simulations reached 0.2 s^{-1} and the normalized myosin accumulation increased fourfold over 200 s, consistent with experimental observations (see Figs. 2 and 5).

The simulations with $k_1 = 14$ s^{-1} reproduced the key features of the experimental observations (Fig. 5). The strain energy E_s^0 associated with cooperative interaction in these simulations was 3 k_BT. Simulations with smaller E_s^0 at 1 and 2 k_BT with different Fd values failed to reproduce the important experimental observations (not shown), suggesting that E_s^0 due to cooperative binding must be larger than 2 k_BT under physiological conditions.

We can now account for the stress-induced accumulation of myosin II to the deformed cortex in the micropipette aspiration experiment. The majority of accumulated myosin
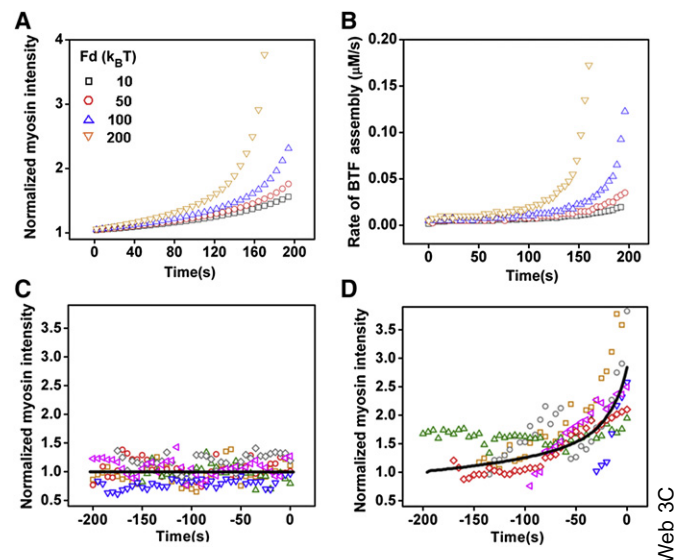

FIGURE 5 BTF assembly and myosin accumulation for different applied forces. The simulated myosin accumulation and accumulation rate for different Fd values are shown in panels *A* and *B*, respectively. Simulations for $Fd = 0$ and 120 k_BT (*solid lines*) are compared to experimental observations (*scattered symbols*) at pressure of 0.2 and 1.0 nN/μm^2 in panels *C* and *D*, respectively. For all simulated cases, $k_1 = 14$ s^{-1} and $E_s^0 = 3$ k_BT (see the Supporting Material for the Fd to pressure conversion). Data from six cells at each pressure are provided to illustrate the range of cellular responses. Experimental and simulation data were aligned at the peak intensities.

diffuses from the cytoplasm to the tip region in the form of myosin monomers (Fig. 6 A), similar to the diffusion of myosin II to the cleavage furrow during cytokinesis. These monomers are then incorporated into the preexisting BTFs or assembled into new BTFs. The in-plane deformation of the actin cortex is greatest in the tip region inside the pipette (35,36). Physically, the associated tension has to decay smoothly away from the tip region because of the gradual change of the cell shape and the continuity of the strain in cortex. We assumed that the tip of the cell has a shape close to a spherical cap and that the cortical tension T is a function
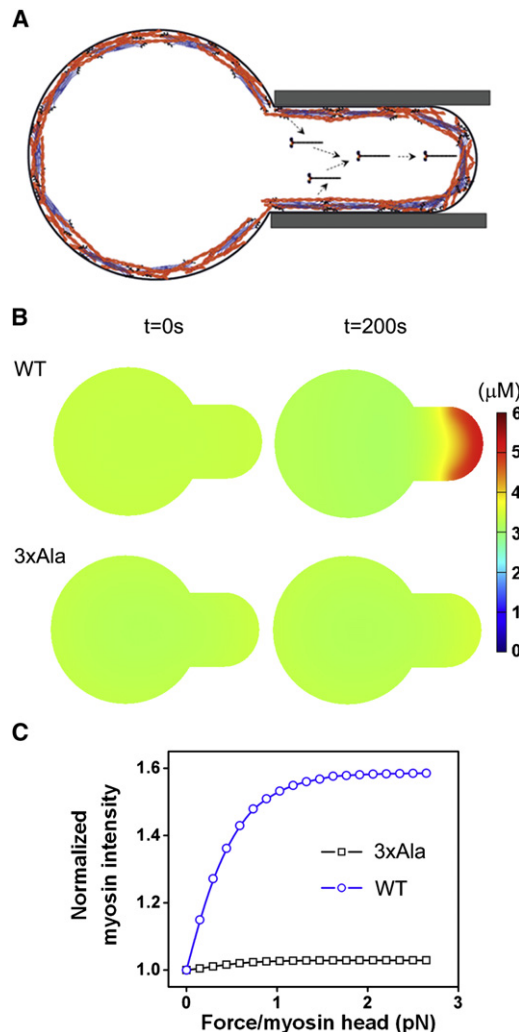

FIGURE 6 Spatial distribution of myosin BTFs in a mechanosensory response. (A) Cartoon diagram of myosin transport due to the spatial bias of force. (B) Spatial concentration of myosin at 200 s, calculated by solving the three-dimensional reaction-diffusion equations for WT myosin II and 3×Ala myosin II mutant. The associated movies for these two-dimensional simulations may be found in Movie S3 and Movie S4 in the Supporting Material. For comparison, a movie (see Movie S5) from a three-dimensional simulation is provided, which showed very similar results. (C) The myosin accumulation increased with the applied force on each myosin head (see Fig. S11 in the Supporting Material for an alternative representation).

of the position along the arc. A simple choice is $T(\theta) = \Delta T \cos \theta$, where θ is the polar angle measured from the tip to the edge (see Fig. S10) and ΔT is the tension drop. The force applied on each myosin head has a similar form: $F(\theta) = \Delta F \cos \theta$, where ΔF is the force drop, corresponding to the tension drop. The nonuniform force distribution profile may then result in different chemical equilibria of the BTF assembly kinetics at each position along the arc, leading to different local levels of myosin accumulation. Following this idea, we substituted the above force profile as boundary conditions into Eq. 3 and solved the three-dimensional reaction-diffusion equations for myosin BTF assembly using COMSOL software (see the Supporting Material).

We also incorporated WT actin polymer concentration along with the 1.1-fold ratio between the 0.5-μm-thick cortex and the cytoplasm (17,28). We then simulated the initial myosin BTF profile and the evolution of the profile over 200 s immediately after the pressure jump for WT myosin II and the constitutively BTF-assembled mutant 3×Ala myosin II (Fig. 6 B; and see Movie S3, Movie S4, and Movie S5). The simulated distributions of WT myosin compare well with the experimental observations (Fig. 2; (3)). Further, the total concentration of myosin II that accumulated was 5 μM, yielding a ratio of normalized intensity of 1.6. This compares favorably with the average normalized ratio and concentrations measured for dividing cells (2,3) and interphase cells (Figs. 2 and 5 and Fig. S2). In contrast, the simulations of 3×Ala did not display notable accumulation, consistent with previous experimental observations (3). The simulated myosin II accumulation also increased with the force in agreement with experimental observations (compare Fig. 6 C and Fig. S11 to Figs. 2 and 5 and Fig. S2).

This modeling scheme only accounts for the rising phase of the myosin accumulation. The falling phase after the peak is likely due to the accumulation of myosin heavy chain kinase C, which accumulates at the micropipette along with myosin II (see Fig. S12). This heavy chain kinase tracks its myosin II substrate, phosphorylating it to promote disassembly (19).

DISCUSSION

To explain how mechanosensitive localization of myosin II occurs, we present a multiscale model based on a myosin bipolar thick filament assembly scheme that incorporates the contributions from cooperative and force-dependent myosin-actin binding. Using physiological protein concentrations and rate constants, our simulations replicate several major in vitro and in vivo experimental observations from the molecular scale to the cell level for both WT and 3×Ala myosin II. Additionally, the simulations provide predictions of the strain energy associated with cooperative binding. Although the simulations draw upon the protein concentrations in *Dictyostelium* cells, the assembly scheme

can be easily adapted for the myosin assembly of other species because the k_1 and k_{-1} that dictate the reactions have reported values in different systems (30), and the concentrations of F-actin and myosin in the cortex are relatively straightforward to measure.

In *Dictyostelium* cells, myosin II and the actin cross-linking protein cortexillin I accumulate at the cleavage furrow during cytokinesis, at the cell rear during motility, and in retracting pseudopods (37,38). The heterocooperativity between myosin and cortexillin proposed here might be one mechanism that contributes to these localized accumulations, and the myosin BTF assembly scheme may be used to understand the kinetics of these dynamic processes. The proposed mechanism of cooperative localization involves conformational changes in the actin filament due, in part, to tension and consistent with this idea, mutant *Dictyostelium* myosin motor domains (S1 fragments) with increased actin affinity localize preferentially to actin filaments in mechanically stressed regions of the cortex (39). Undoubtedly, the principles described here are general and may be applicable to other myosin-mediated, force-dependent accumulation of heterologous proteins, such as in focal adhesions (40).

Overall, we provide a multiscale model that accounts for the in vivo cellular scale mechanosensitive accumulation of myosin II from the cooperative binding of the motor domain coupled to the assembly of bipolar thick filaments.

SUPPORTING MATERIAL

Additional sections with supporting equations, three tables, 12 figures, and five movies are available at http://www.biophysj.org/biophysj/supplemental/S0006-3495(11)05422-1.

GFP-MHCKC plasmid is a gift from Tom Egelhoff.

REFERENCES

1. Spudich, J. A. 2001. The myosin swinging cross-bridge model. *Nat. Rev. Mol. Cell Biol.* 2:387–392.

2. Effler, J. C., Y.-S. Kee, …, D. N. Robinson. 2006. Mitosis-specific mechanosensing and contractile protein redistribution control cell shape. *Curr. Biol.* 16:1962–1967.

3. Ren, Y., J. C. Effler, …, D. N. Robinson. 2009. Mechanosensing through cooperative interactions between myosin II and the actin cross-linker cortexillin I. *Curr. Biol.* 19:1421–1428.

4. Wozniak, M. A., and C. S. Chen. 2009. Mechanotransduction in development: a growing role for contractility. *Nat. Rev. Mol. Cell Biol.* 10:34–43.

5. Greene, L. E., and E. Eisenberg. 1980. Cooperative binding of myosin subfragment-1 to the actin-troponin-tropomyosin complex. *Proc. Natl. Acad. Sci. USA.* 77:2616–2620.

6. Trybus, K. M., and E. W. Taylor. 1980. Kinetic studies of the cooperative binding of subfragment 1 to regulated actin. *Proc. Natl. Acad. Sci. USA.* 77:7209–7213.

7. Orlova, A., and E. H. Egelman. 1997. Cooperative rigor binding of myosin to actin is a function of F-actin structure. *J. Mol. Biol.* 265:469–474.

8. Veigel, C., J. E. Molloy, …, J. Kendrick-Jones. 2003. Load-dependent kinetics of force production by smooth muscle myosin measured with optical tweezers. *Nat. Cell Biol.* 5:980–986.

9. Uyeda, T. Q., P. D. Abramson, and J. A. Spudich. 1996. The neck region of the myosin motor domain acts as a lever arm to generate movement. *Proc. Natl. Acad. Sci. USA.* 93:4459–4464.

10. Bobkov, A. A., A. Muhlrad, …, E. Reisler. 2006. Cooperative effects of cofilin (ADF) on actin structure suggest allosteric mechanism of cofilin function. *J. Mol. Biol.* 356:325–334.

11. De La Cruz, E. M., and D. Sept. 2010. The kinetics of cooperative cofilin binding reveals two states of the cofilin-actin filament. *Biophys. J.* 98:1893–1901.

12. Shin, H., K. R. Purdy Drew, …, G. M. Grason. 2009. Cooperativity and frustration in protein-mediated parallel actin bundles. *Phys. Rev. Lett.* 103:238102.

13. Galkin, V. E., A. Orlova, and E. H. Egelman. 2011. Actin filaments as tension sensors. *Curr. Biol.* In press.

14. Siddique, M. S. P., G. Mogami, …, M. Suzuki. 2005. Cooperative structural change of actin filaments interacting with activated myosin motor domain, detected with copolymers of pyrene-labeled actin and acto-S1 chimera protein. *Biochem. Biophys. Res. Commun.* 337:1185–1191.

15. Mahajan, R. K., K. T. Vaughan, …, J. D. Pardee. 1989. Actin filaments mediate *Dictyostelium* myosin assembly in vitro. *Proc. Natl. Acad. Sci. USA.* 86:6161–6165.

16. MacKintosh, F. C. 2011. Active gels: motors keep dynamics steady. *Nat. Mater.* 10:414–415.

17. Surcel, A., Y.-S. Kee, …, D. N. Robinson. 2010. Cytokinesis through biochemical-mechanical feedback loops. *Semin. Cell Dev. Biol.* 21:866–873.

18. Bao, G., and S. Suresh. 2003. Cell and molecular mechanics of biological materials. *Nat. Mater.* 2:715–725.

19. Yumura, S., M. Yoshida, …, T. T. Egelhoff. 2005. Multiple myosin II heavy chain kinases: roles in filament assembly control and proper cytokinesis in *Dictyostelium*. *Mol. Biol. Cell.* 16:4256–4266.

20. Schmit, J. D., E. Kamber, and J. Kondev. 2009. Lattice model of diffusion-limited bimolecular chemical reactions in confined environments. *Phys. Rev. Lett.* 102:218302.

21. Landau, L. D., and E. M. Lifshitz. 1986. Theory of Elasticity. Elsevier, Oxford, UK.

22. Tokuraku, K., R. Kurogi, …, T. Q. Uyeda. 2009. Novel mode of cooperative binding between myosin and Mg^{2+}-actin filaments in the presence of low concentrations of ATP. *J. Mol. Biol.* 386:149–162.

23. Murphy, C. T., and J. A. Spudich. 1998. *Dictyostelium* myosin 25–50K loop substitutions specifically affect ADP release rates. *Biochemistry.* 37:6738–6744.

24. Uehara, R., G. Goshima, …, E. R. Griffis. 2010. Determinants of myosin II cortical localization during cytokinesis. *Curr. Biol.* 20:1080–1085.

25. Mahajan, R. K., and J. D. Pardee. 1996. Assembly mechanism of *Dictyostelium* myosin II: regulation by K$^+$, Mg^{2+}, and actin filaments. *Biochemistry.* 35:15504–15514.

26. Sinard, J. H., W. F. Stafford, and T. D. Pollard. 1989. The mechanism of assembly of *Acanthamoeba* myosin-II minifilaments: minifilaments assemble by three successive dimerization steps. *J. Cell Biol.* 109:1537–1547.

27. Moores, S. L., and J. A. Spudich. 1998. Conditional loss-of-myosin-II-function mutants reveal a position in the tail that is critical for filament nucleation. *Mol. Cell.* 1:1043–1050.

28. Reichl, E. M., Y. Ren, …, D. N. Robinson. 2008. Interactions between myosin and actin crosslinkers control cytokinesis contractility dynamics and mechanics. *Curr. Biol.* 18:471–480.

29. Berlot, C. H., P. N. Devreotes, and J. A. Spudich. 1987. Chemoattrac-tant-elicited increases in *Dictyostelium* myosin phosphorylation are due to changes in myosin localization and increases in kinase activity. *J. Biol. Chem.* 262:3918–3926.

30. Takács, B., E. O'Neall-Hennessey, …, M. Kovács. 2011. Myosin cleft closure determines the energetics of the actomyosin interaction. *FASEB J.* 25:111–121.

31. Kovacs, M., K. Thirumurugan, …, J. R. Sellers. 2007. Load-dependent mechanism of nonmuscle myosin 2. *Proc. Natl. Acad. Sci. USA.* 104:9994–9999.

32. Ben-Naim, A. 2001. Cooperativity and Regulation in Biochemical Processes. Kluwer Academic/Plenum Publishers, New York.

33. Cao, W., J. P. Goodarzi, and E. M. De La Cruz. 2006. Energetics and kinetics of cooperative cofilin-actin filament interactions. *J. Mol. Biol.* 361:257–267.

34. Zhou, Q., Y.-S. Kee, …, D. N. Robinson. 2010. 14–3-3 coordinates microtubules, rac, and myosin II to control cell mechanics and cytoki-nesis. *Curr. Biol.* 20:1881–1889.

35. Discher, D. E., D. H. Boal, and S. K. Boey. 1998. Simulations of the erythrocyte cytoskeleton at large deformation. II. Micropipette aspira-tion. *Biophys. J.* 75:1584–1597.

36. Derényi, I., F. Jülicher, and J. Prost. 2002. Formation and interaction of membrane tubes. *Phys. Rev. Lett.* 88:238101.

37. Moores, S. L., J. H. Sabry, and J. A. Spudich. 1996. Myosin dynamics in live *Dictyostelium* cells. *Proc. Natl. Acad. Sci. USA.* 93:443–446.

38. Xiong, Y., C. Kabacoff, …, P. Iglesias. 2010. Automated characteriza-tion of cell shape changes during amoeboid motility by skeletonization. *BMC Syst. Biol.* 4:33.

39. Uyeda, T. Q. P., Y. Iwadate, …, S. Yumura. 2011. Stretching actin fila-ments within cells enhances their affinity for the myosin II motor domain. *PLoS ONE.* 6:e26200.

40. Kuo, J.-C., X. Han, …, C. M. Waterman. 2011. Analysis of the myosin-II-responsive focal adhesion proteome reveals a role for β-Pix in negative regulation of focal adhesion maturation. *Nat. Cell Biol.* 13:383–393.

Understanding the Cooperative Interaction between Myosin II and Actin Crosslinkers Mediated by Actin Filaments during Mechanosensation

Tianzhi Luo, Krithika Mohan, Vasudha Srivastava, Yixin Ren, Pablo A. Iglesias, and Douglas N. Robinson

Supplemental Materials

Supplemental Methods, Analysis, and Discussion

Pharmacological modulation of F-actin levels and the corresponding myosin mechanosensory responses

We used latrunculin-A and jasplakinolide to adjust the F-actin level in *myoII* null cells expressing GFP-myosin II and determined the amount of F-actin by rhodamine-phalloidin staining. Cells were grown overnight in the presence of 0.2% DMSO on coverslips, and were then treated with 5 μM latrunculin-A or 2 μM jasplakinolide for 20 min. The cells were fixed with -20°C acetone for 3 min. on ice and blocked in 1X PBT (1X PBS, 0.05% Triton X-100 and 0.5% BSA). Samples were stained with 160 nM rhodamine-phalloidin for 1 hour, then washed 4-5 times with 1X PBT and mounted in 90% glycerol 1X PBS. For quantification of the actin levels, images were acquired on an Olympus IX81 microscope under identical imaging conditions. The fluorescence signals were measured for each cell and used as an indicator of the relative F-actin amount. More than 300 cells were counted per condition and the signals were normalized to the average of the 0.2% DMSO control. The cells were also imaged using a Zeiss 510 Meta confocal microscope to study the effects on the actin and myosin II distributions.

Latrunculin treatment reduced the F-actin levels to 40% of control while jasplakinolide treatment increased F-actin levels four-fold (Fig. S2A,B). Both drug treatments induced aggregations of F-actin and myosin II in the cortex, which lead to the structural non-uniformity as compared to untreated cells. In the MPA assays, only very low pressures could be applied to latrunculin-A-treated cells due to their extremely high deformability (higher pressures aspirated the entire cell into the micropipette, making measurements at these pressures impossible). No mechanosensitive accumulation was observed at these low pressures. In contrast, jasplakinolide treatment did not alter the mechanoresponsiveness as compared to control over a range of aspiration pressures (Fig. S2C).

The 2D kinetic Monte Carlo simulations reflect the 3D events

In the lattice kinetic Monte Carlo simulations, we used a 2D simulation box. However, the simulations reasonably mimic 3D events because the length of mesh size, the length that single myosin covers along actin filament, the binding and unbinding rates, and the diffusion coefficients are based on 3D structures and 3D measurements (1). As far as the diffusion in different dimensions is concerned, the mean square displacements of a random walk during time period Δt are $\langle \Delta x \rangle^2 = 4D\Delta t$ and $\langle \Delta x \rangle^2 = 6D\Delta t$ for 2D and 3D cases, respectively, and hence the mean square displacement differs only by a factor of 1.5 between the 2D and 3D cases. However, differences between these 2D and 3D scenarios could slightly alter the cluster size.

The mean-field approximation of E_s from statistical mechanics

We considered a one-dimensional actin filament with N binding sites for myosin and used periodic boundary conditions to mimic an infinitely long filament. The partition function Z of the system at each ϕ was calculated from 10^7 random samplings according to $Z = \sum_j g_j \exp\left(-H_j/k_B T\right)$, where g_j is the corresponding degeneracy of the same energy level and H is the energy of the system defined as $H = U - E_{binding}$. Here, U is the free energy of the system in the absence of the binding of myosin to actin and $E_{binding}$ is the binding energy of the system. Mathematically, U has the form of $U = NE_{site} + N\phi E_{myo}$, where $N\phi$ gives the number of myosins in the system, and E_{site} and E_{myo} are the energies for the single binding site and myosin, respectively. The binding energy of the system is simply the sum of the binding energy of each myosin-actin complex that has been defined in the KMC scheme, *i.e.*, $E_{binding} = \sum_i \left(E_i^0 + \Delta E_i\right)$ and $\Delta E_i = \sum_k E_s^k(x_{ik})$ for $1 \leq i \leq N\phi$. The system energy H then depends on the coverage ϕ.

The probability of the system at energy level H_j is $P_j(H_j) = \frac{1}{Z} g_j \exp\left(-H_j/k_B T\right)$ and the mean value of H is $\langle H \rangle = \sum_j P_j H_j$. It is noted that U and E_i^0 are constants for each $N\phi$ and do not depend on the permutation of the myosin positions. As a result, they cancel out eventually in the

exponential terms in both the numerator and the denominator of P_j. By expanding both sides of $\langle H \rangle = \sum_j P_j H_j$, one has

$$\left\langle U - \sum_i E_i^0 - \sum_i \Delta E_i \right\rangle = \frac{\sum_j g_j \left(U - \sum_i E_i^0 - \sum_i \Delta E_i \right)_j \exp\left(\left(\sum_i \Delta E_i \right)_j \Big/ k_B T \right)}{\sum_j g_j \exp\left(\left(\sum_i \Delta E_i \right)_j \Big/ k_B T \right)}. \qquad \text{(S1)}$$

Again, considering that U and E_i^0 are constants, Eq. S1 reduces to

$$\left\langle \sum_i \Delta E_i \right\rangle = \frac{\sum_j g_j \left(\sum_i \Delta E_i \right)_j \exp\left(\left(\sum_i \Delta E_i \right)_j \Big/ k_B T \right)}{\sum_j g_j \exp\left(\left(\sum_i \Delta E_i \right)_j \Big/ k_B T \right)}. \qquad \text{(S2)}$$

$\left\langle \sum_i \Delta E_i \right\rangle$ is the average change in the binding energy of the system due to the cooperative interactions. Since $\sum_i \Delta E_i = \sum_i E_s^i(x_{ik}) = \sum_i \sum_k E_s^0 \exp\left(-|x_{ik}|/\lambda \right)$, the mean-field approximation of $\sum_i \Delta E_i$, E_s, can be calculated exactly for each $N\phi$ using Eq. S2 and the values of E_s^0 and λ.

The effect of the distribution of actin filament length on the cooperativity of myosin II

The mesh size of actin network is an average distance between the crosslinking points. In 2D lattice kinetic Monte Carlo simulations, the window size of simulation box is equal to the mesh size assumed. When the mesh size is much larger than the characteristic decay length of the strain field, λ, changing the mesh size only affects the effective actin concentration in the simulation box and does not qualitatively change the cooperativity between bound myosins. However, in cells, the actin filament length has a broad distribution, varying from a few nanometers to submicron or even microns. If the length of certain actin filaments is close to the decay length, λ ($3a = 15$ nm), the cooperativity of myosins on these filaments will not be as strong as predicted (or simulated) by this paper. To compare the simulation results in this paper to the myosin behaviors in real cells, it is necessary to take the distribution of actin filament length into account. For WT *Dictyostelium* cells, the mean and the median of the actin filament length are 94 nm and 81 nm, respectively (2). Therefore, the effect of the randomness of actin

3

filament lengths is negligible when we compare the simulations to the experiments with *Dictyostelium* cells.

The possibility of the force-dependency of the on-rate, k_1

Here, the "off" rates k_{-1} is considered to be the primary force dependent term for two reasons. The first is that the *in vitro* assay in Ref. (3) indicates the cooperativity of myosin II is dependent on the isometric, actin-bound state of myosin II. The second is that the myosin actin-binding lifetime is force-dependent (4). These two findings strongly suggest that the "off" rates (or the binding lifetimes of myosin to actin) are force-dependent. However, it is possible that the strain energy also affects the "on" rates by altering the actin filament structure, promoting myosin binding. Numerically, we can simulate the cooperativity associated with the changes of the "on" rates. However, with limited experimental evidence for changes in the "on" rate due to forces and strains, the biological relevance of such simulations is unclear.

The dependence of $\Delta E_b'$ on m

According to Eq. 3 (main text), k_{-1} is an exponential function of $\Delta E_b'$, which is a function of the amount of bound myosin (m) and is described by

$$\Delta E_b' = \delta m + Fd/\alpha m . \tag{S3}$$

The first term represents the strain energy and the second term is associated with the applied force. δ can have a value of either δ_1 or δ_2 depending on the amount of bound myosin m according to Eq. 3. $\delta_1 > \delta_2$ is always true since $\chi_1 > \chi_2$. $\Delta E_b'$ reaches its minimum when m is at its critical value $m_{cr} = \sqrt{\alpha Fd/\delta}$. δ_{cr} may be defined as $\delta_{cr} = Fd/\alpha m_{cr}^2$. When $\delta > \delta_{cr}$, $\Delta E_b'$ increases with m and otherwise decreases with m. As a result, k_{-1} decreases with m if $\delta > \delta_{cr}$ and increases with m if $\delta < \delta_{cr}$. We then considered the case where $\delta_1 > \delta_{cr} > \delta_2$. Two curves (dotted lines) describing $\Delta E_b'$ as a function of ϕ are shown in Fig. S6A with $\delta = \delta_1$ and $\delta = \delta_2$, respectively. It is easier to discuss the dependence of $\Delta E_b'$ on m instead of ϕ as m is related to ϕ by $\phi = 3m/C_{actin}$. During myosin assembly, E_s initially has a slope of δ_1 at ϕ and the slope changes to δ_2 as the number of bound myosin ϕ exceeds ϕ^*. The corresponding transient

behavior of $\Delta E_b'$ is schematically indicated by the solid curve in Fig. 3A. $\Delta E_b'$ as a function of ϕ at different Fd/α for E_s^0 at 1, 2, and $3k_BT$ are shown in Figs S6B-D, respectively.

The concentration of unbound myosin monomer during myosin transport

In cells, the local myosin concentration changes but the concentration of certain myosin forms might be constant. The mobile or diffusible unit of myosin in cell cortex is more likely to be the unbound myosin monomer (UMM). The cytoplasm can be considered as a reservoir of UMM and diffusion is able to quickly smooth the UMM gradient in the cytoplasm, which means the concentration of UMM is constant during the BTF assembly induced by local force. Therefore, to simulate the myosin accumulation and BTF assembly during mechanosensing without using real 3D geometry (results shown in Fig. 5), the concentration of UMM (M and $\overline{M}$) is kept constant.

The sensitivity of k_- and k_+ in the absence of force

The coefficient k_- may be evaluated numerically by fitting the simulation results to the observation that the BTF fraction is ~20%-50%. Here, k_- varied in the range 0.004-0.1 s^{-1} assuming $C_{myosin} = 3.4$ μM, $C_{actin} = 20.0$ μM, $E_s^0 = 1.0 k_BT$, and $Fd = 0$ (Fig. S7A). It can be seen that high k_- leads to less assembled BTF. At $k_- = 0.1$ s^{-1}, the BTF concentration is maintained at 0.7 μM, ~20% of the total myosin. For the case of $E_s^0 > 1.0 k_BT$, larger k_- is needed to set steady-state BTF at 0.7 μM (not shown).

As a proof of principle, k_+ is varied by adjusting C_{actin} in the range of 5-20 μM, assuming that $C_{myosin} = 3.4$ μM, $k_- = 0.1$ s^{-1}, $E_s^0 = 1.0$ k_BT, and $Fd = 0$ (Fig. S7B). It can be seen that the high F-actin does promote BTF assembly and the saturation concentration of actin is about six times the myosin concentration, which is consistent with the experimental observations (5). For different E_s^0, it is true that higher k_+ leads to more bound myosin, which can be seen by comparing Fig. S8A to S8B. In these simulations, the force term is zero and the myosin concentration is constant. Hence, the simulations reflect the conditions of *in vitro* BTF assembly.

Estimation of the Fd **term for** *Dictyostelium* **cells during MPA measurements**

During MPA measurements, the applied pressure is transmitted through the membrane and the membrane-cortex linkage to the actin cortex. Initially, myosin II concentration in the cortex, C_{myosin}, is 4 μM of which approximately half is in BTFs (6). Assuming the thickness of the cortex is ~0.5 μm, ~2000 myosins per μm^2 counteract the pressure applied externally on the plasma membrane. Each myosin has two heads and a 4.0 pN stall force. As a result, the upper bound of duty ratio, 0.06, gives a maximum stress of ~0.5 nN/μm^2 if all engaged myosins are stalled due to the applied force. This leads to a corresponding maximum value of Fd of ~280 k_BT where Fd is based on the total force/area (nN/μm^2).

The relation between Fd **term and the applied pressure during MPA measurements**

Besides myosin II, a number of other load bearing units exist in the actin cytoskeleton, including actin crosslinking proteins whose concentrations are also on the order of 1 μM. Because these proteins bear some of the load, only a fraction of the applied pressure is distributed on myosin. Based on measurements of the cortical tension in interphase wild type and *myoII* null cells (2), we estimate that myosin II contributes ~20% of the cortical tension. Thus, it is reasonable to assume that myosin II only bears ~20% of the pressure applied on interphase wild type *Dictyostelium* cells during MPA measurements. Further support for this idea comes from the observation that reducing interphase cortical tension by 3-fold in *racE* mutants reduces the mechanosensitive pressure-range of interphase cells by 3-5-fold (RacE controls the distribution of cortical actin crosslinking proteins) (7). Therefore, the range of 0~280 k_BT of Fd for myosin II roughly corresponds to 0~2.5 nN/μm^2 (*i.e.*, the maximum is five times ~0.5 nN/μm^2) of the applied pressure on the intact wild type cytoskeleton when the cortical myosin II concentration is 4 μM.

Solving the reaction-diffusion equations of myosin BTF assembly and myosin accumulation in 3D geometry by COMSOL

The multi-scale model describing the BTF assembly formation and myosin accumulation was implemented using COMSOL Multi-physics (COMSOL, Burlington, MA) version 4.2. The model was configured using a geometry drawn in "2D and 2D" axially symmetric space, to take advantage of symmetry. Subsequent results were displayed in full three dimensions. Each simulation was meshed using a physics controlled "Normal mesh." The reaction-diffusion

6

equations describing the model were solved using the Coefficient Form Partial Differential Equation (PDE) Interface found under the Mathematics branch of Physics Interfaces, along with a zero flux boundary condition. The system of PDEs were first solved at steady state using the Multifrontal Massively Parallel Sparse (MUMPS) direct solver and the resultant solution set was used as the initial condition for subsequent simulations. For simulating transient behavior the MUMPS direct solver along with a Backward Differentiation Formula (BDF) time stepping method was used. The time step for every computation was allowed to be chosen by the solver through the "Free" time-stepping option, but the maximum time-step chosen by the solver was fixed to 0.1s. The total simulation time was set to 200 s. For all the numerical simulations, COMSOL Multi-physics accepts volume concentrations (μM) in SI derived units, so all concentrations were converted to mol/m^3 by multiplying (or dividing) by 10^{-3}. For simplicity, the maximum size of BTF in the simulations is n=5 although it was found experimentally that n could be as large as 36. The cell diameter was 10 μm. The diameter of the pipette was 5 μm and the length of the cylindrical part was 2.5 μm (Fig. S10). A diffusion coefficient 0.2 μm^2/s (1), was chosen for all myosin forms except for BTF$_4$ and BTF$_5$ for which the diffusion coefficient was set to zero. The thickness of the actin cortex is 500 nm. The change of k_{-1} due to applied force was only applied to the actin cortex in the tip region.

The reaction-diffusion equations in the simulations are

$$\frac{\partial C_M}{\partial t} = D\frac{\partial^2 C_M}{\partial \vec{x}^2} + (k_{-1}C_{M^*} - k_1 C_M) + \left(k_+ C_{\overline{M}} - k_- C_M\right)$$

$$\frac{\partial C_{\overline{M}}}{\partial t} = D\frac{\partial^2 C_{\overline{M}}}{\partial \vec{x}^2} + (k_1 C_{\overline{M}^*} - k_{-1}C_{\overline{M}}) - \left(k_+ C_{\overline{M}} - k_- C_M\right)$$

$$\frac{\partial C_{\overline{M}^*}}{\partial t} = D\frac{\partial^2 C_{\overline{M}^*}}{\partial \vec{x}^2} + (k_{-1}C_{\overline{M}^*} - k_1 C_{\overline{M}}) - \left(k_+ C_{\overline{M}^*} - k_- C_{M^*}\right)$$

$$\frac{\partial C_{M^*}}{\partial t} = D\frac{\partial^2 C_{M^*}}{\partial \vec{x}^2} + (k_1 C_M - k_{-1}C_{M^*}) + \left(k_+ C_{\overline{M}^*} - k_- C_{M^*}\right) - 2\left(k_2 C_{M^*}^2 - k_{-2}C_D\right)$$

$$\frac{\partial C_D}{\partial t} = D\frac{\partial^2 C_D}{\partial \vec{x}^2} + (k_2 C_M^2 - k_{-2}C_D) - 2\left(k_3 C_D^2 - k_{-3}C_T\right) - \left(k_4 C_D C_T - k_{-4}C_{BTF_3}\right) \quad , \qquad \text{(S4)}$$
$$- \left(k_5 C_D C_{BTF_3} - k_{-5}C_{BTF_4}\right) - \left(k_5 C_D C_{BTF_4} - k_{-5}C_{BTF_5}\right)$$

$$\frac{\partial C_T}{\partial t} = D\frac{\partial^2 C_T}{\partial \vec{x}^2} + (k_3 C_D^2 - k_{-3}C_T) - \left(k_4 C_D C_T - k_{-4}C_{BTF_3}\right)$$

$$\frac{\partial C_{BTF_4}}{\partial t} = D\frac{\partial^2 C_{BTF_4}}{\partial \vec{x}^2} + (k_5 C_D C_{BTF_3} - k_{-5}C_{BTF_4}) - \left(k_5 C_D C_{BTF4} - k_{-5}C_{BTF_5}\right)$$

$$\frac{\partial C_{BTF_5}}{\partial t} = D\frac{\partial^2 C_{BTF_5}}{\partial \vec{x}^2} + (k_5 C_D C_{BTF_4} - k_{-5}C_{BTF_5})$$

where C represents the concentration and the subscripts correspond to different components in the assembly scheme. Parameters and algorithm are listed in Tables S1 to S3.

Supplemental References

1. Uehara, R., G. Goshima, I. Mabuchi, R. D. Vale, J. A. Spudich, and E. R. Griffis. 2010. Determinants of myosin II cortical localization during cytokinesis. Curr. Biol. 20:1080-1085.
2. Reichl, E. M., Y. Ren, M. K. Morphew, M. Delannoy, J. C. Effler, K. D. Girard, S. Divi, P. A. Iglesias, S. C. Kuo, and D. N. Robinson. 2008. Interactions between myosin and actin crosslinkers control cytokinesis contractility dynamics and mechanics. Curr. Biol. 18:471 - 480.
3. Tokuraku, K., R. Kurogi, R. Toya, and T. Q. Uyeda. 2009. Novel mode of cooperative binding between myosin and Mg2+ -actin filaments in the presence of low concentrations of ATP. J. Mol. Biol. 386:149-162.
4. Veigel, C., J. E. Molloy, S. Schmitz, and J. Kendrick-Jones. 2003. Load-dependent kinetics of force production by smooth muscle myosin measured with optical tweezers. Nat. Cell Biol. 5:980-986.
5. Mahajan, R. K., K. T. Vaughan, J. A. Johns, and J. D. Pardee. 1989. Actin filaments mediate *Dictyostelium* myosin assembly in vitro. Proc. Natl. Acad. Sci. U.S.A. 86:6161-6165.
6. Surcel, A., Y.-S. Kee, T. Luo, and D. N. Robinson. 2010. Cytokinesis through biochemical-mechanical feedback loops. Semin. Cell Dev. Biol. 21:866-873.
7. Ren, Y., J. C. Effler, M. Norstrom, T. Luo, R. A. Firtel, P. A. Iglesias, R. S. Rock, and D. N. Robinson. 2009. Mechanosensing through cooperative interactions between myosin II and the actin crosslinker cortexillin I. Curr. Biol. 19:1421-1428.
8. Berlot, C. H., P. N. Devreotes, and J. A. Spudich. 1987. Chemoattractant-elicited increases in Dictyostelium myosin phosphorylation are due to changes in myosin localization and increases in kinase activity. J. Biol. Chem. 262:3918-3926.
9. Mahajan, R. K., and J. D. Pardee. 1996. Assembly mechanism of *Dictyostelium* myosin II: Regulation by K^+, Mg^{2+}, and actin filaments. Biochemistry 35:15504-15514.
10. Moores, S. L., and J. A. Spudich. 1998. Conditional loss-of-myosin-II-munction mutants reveal a position in the tail that Is critical for filament nucleation. Mol. Cell 1:1043-1050.
11. Yumura, S., M. Yoshida, V. Betapudi, L. S. Licate, Y. Iwadate, A. Nagasaki, T. Q. Uyeda, and T. T. Egelhoff. 2005. Multiple myosin II heavy chain kinases: roles in filament assembly control and proper cytokinesis in *Dictyostelium*. Mol. Biol. Cell 16:4256-4266.
12. Takcás, B., E. O'Neall-Hennessey, C. Hetényi, J. Kardos, A. G. Szent-Györgyi, and M. Kovács. 2011. Myosin cleft closure determines the energetics of the actomyosin interaction. FASEB J. 25:111-121.
13. Zhou, Q., Y.-S. Kee, C. C. Poirier, C. Jelinek, J. Osborne, S. Divi, A. Surcel, M. E. Will, U. S. Eggert, A. Müller-Taubenberger, P. A. Iglesias, R. J. Cotter, and D. N. Robinson. 2010. 14-3-3 coordinates microtubules, rac, and myosin II to control cell mechanics and cytokinesis. Curr. Biol. 20:1881-1889.

Table S1. Constants.

Parameter	Value	Conversion to SI derived units	Description	Reference
D	0.2 µm²/s	2×10^{-13} m²/s	Diffusion coefficient	(1)
k_+	0.05 s⁻¹	0.05 s⁻¹	Scheme, Fig. 1	(8)
k_{-1}^0	300 s⁻¹	300 s⁻¹	Scheme, Fig. 1: Rate controlling conversion from bound and unbound states of myosin monomers in the absence of force and homo-cooperativity	(9)
k_2	0.37 µM⁻¹s⁻¹	370 m³/mol·s	Scheme, Fig. 1	(10)
k_{-2}	0.01 s⁻¹	0.01 s⁻¹	Scheme, Fig. 1	Our estimate
k_3	0.0395 µM⁻¹s⁻¹	39.5 m³/mol·s	Scheme, Fig. 1	(10)
k_{-3}	0.045 s⁻¹	0.045 s⁻¹	Scheme, Fig. 1	(9)
k_4	1.25 µM⁻¹s⁻¹	1250 m³/mol·s	Scheme, Fig. 1	(9)
k_{-4}	0.025 s⁻¹	0.025 s⁻¹	Scheme, Fig. 1	(9)
k_5	10 µM⁻¹s⁻¹	10,000 m³/mol·s	Scheme, Fig. 1	Our estimate
k_{-5}	0.2 s⁻¹ (for WT) or 0.005 s⁻¹ (for 3xAla)	0.2 s⁻¹ / 0.005 s⁻¹	Scheme, Fig. 1	(2, 11, 13)
k_{on}	0.45 µM⁻¹s⁻¹	450 m³/mol·s	On rate for myosin binding to actin	(12)
C_{actin}	72 µM	72×10^{-3} mol/m³	Actin concentration in the cytosol	(6)
C_{actin_cortex}	79 µM	79×10^{-3} mol/m³	Actin concentration in the cortex	(6)
$C_{myo\ total}$	3.4 µM	3.4×10^{-3} mol/m³	Total cellular myosin II concentration	(6)
α	36 µM⁻¹	36×10^{-6} M⁻¹	The product of the duty ratio, a geometric factor and the Avogadro's number	(6)

Table S2. Variables.

Parameter	Method of evaluation	Description
k_{-}	Evaluated numerically by fitting simulation results to the observation that $C_{\text{myo BTF}}$ = ~ 20-50% of $C_{\text{myo Total}}$ (ref.(13))	Scheme, Fig. 1: Myosin tail phosphorylation rate
k_1	$k_{on} C_{\text{actin}}$	Scheme, Fig. 1: Rate controlling conversion from bound and unbound states of myosin monomers
k_{-1}	$k_{-1}^{0} \exp(-\Delta E_b^{'}(x, y, t) / k_B T)$	Scheme, Fig. 1: Rate controlling conversion from bound and unbound states of myosin monomers

Table S3. Algorithm for calculating k_{-1}.

$$k_{-1}(x,y,t) = k_{-1}^0 \exp(-\Delta E_b'(x,y,t)/k_B T)$$

$$\Delta E_b'(x,y,t) = E_s + \frac{Fd(\theta)}{\alpha m(x,y,t)}$$

$$E_s = \begin{cases} \chi_1 \varphi \\ \chi_1 \varphi^* + \chi_2(\varphi - \varphi^*) \end{cases}$$

where χ_1, χ_2, and φ^* are derived from Fig. S5C.

$$\varphi = \frac{3m(x,y,t)}{C_{actin}}$$

$$Fd(\theta) = Fd_0 \cos(\theta)$$

where $\cos(\theta) = \cos(\arctan(y,x))$, and Fd_0 is the energy associated with the maximum applied stress at the cortex by micropipette aspiration.

$$m(x,y,t) = M^* + \overline{M}^* + 2D^* + 4T^* + \sum_n BTF_n^*$$
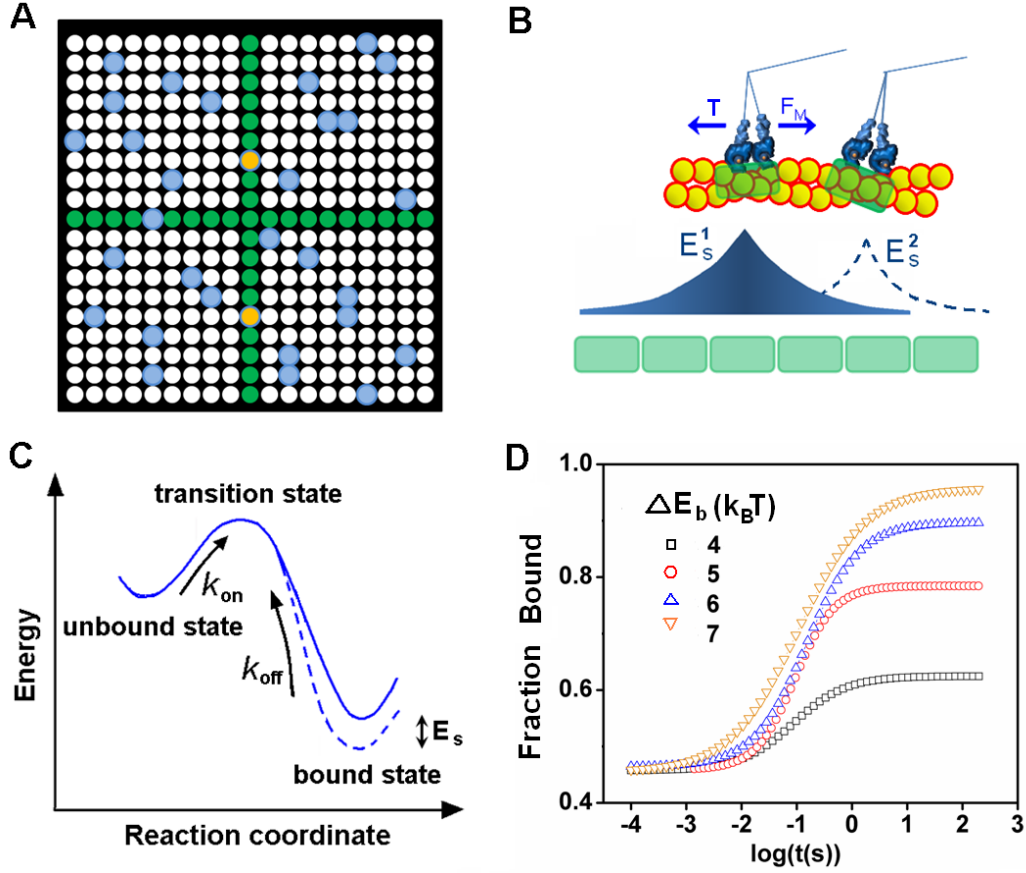
Figure S1. Kinetic Monte Carlo model for cooperative myosin binding to actin filaments. (A) A schematic graph of the 2D lattice for the KMC simulation is shown. White dots are empty lattices. Green dots are available binding sites. Yellow dots and blue dots represent bound and unbound myosins. (B) The exponentially decaying strain field associated with binding. The binding sites are indicated by green blocks. (C) The energy landscape of myosin binding to actin. E_s is the change of binding energy due to strain. (D) The kinetic binding curves of myosins for different changes of binding energy due to cooperative binding are shown.
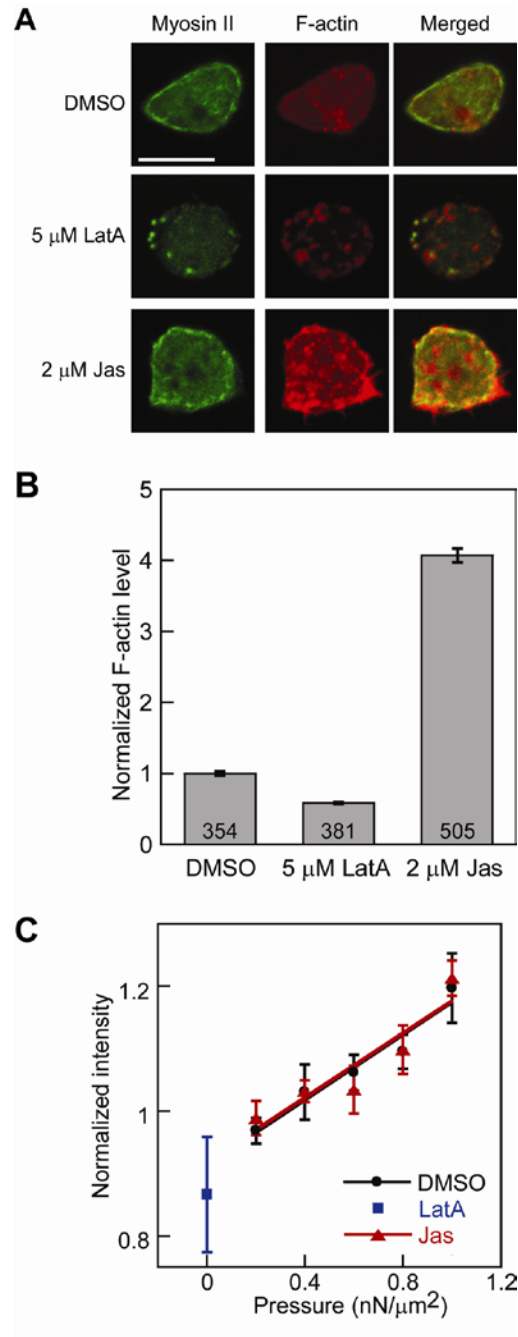
Figure S2. Adjustment of the myosin II cortical localization and its mechanosensory response using actin inhibitors. (A) Confocal images of GFP-myosin II and rhodamine-phalloidin stained F-actin in fixed cells treated by 5 μM latrunculin and 2 μM jasplakinolide. Scale bar represents 10 µm. (B) The quantified F-actin levels for different drug treatments (the number of cells measured per condition is listed on the histogram). (C) The mechanosensory response of myosin with different drug treatments at different pressures. At each pressure, the data point (mean±SEM) represents measurements from 15-20 cells.
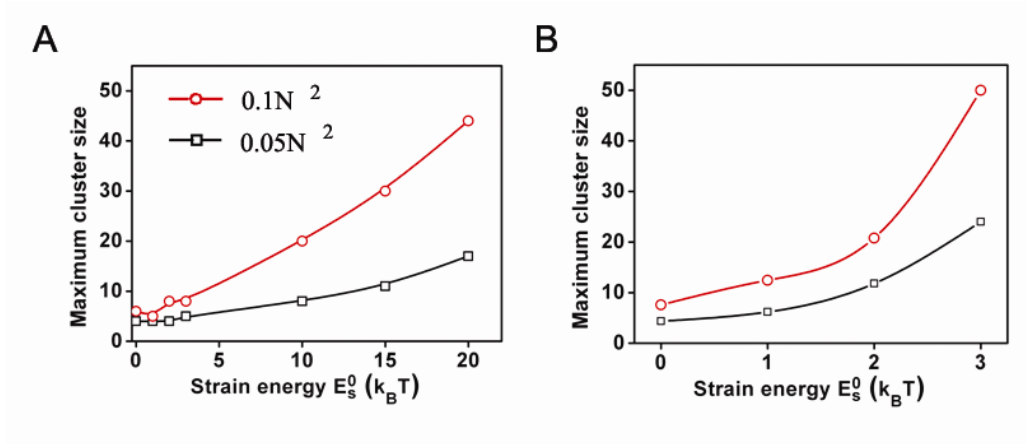
Figure S3. The nearest-neighbor interaction underestimates the effect of cooperativity on myosin binding to F-actin. The maximum cluster size of bound myosin in 2D lattice KMC simulations with nearest-neighbor interaction (*i.e.*, $|x_{ij}| = a$), and long-range interactions (for example, $|x_{ij}| \leq 3a$) are shown in (A) and (B), respectively. The myosin concentration is expressed in units of the simulation window size, N. Here, N=128, and the legend insert applies to both panels.

15
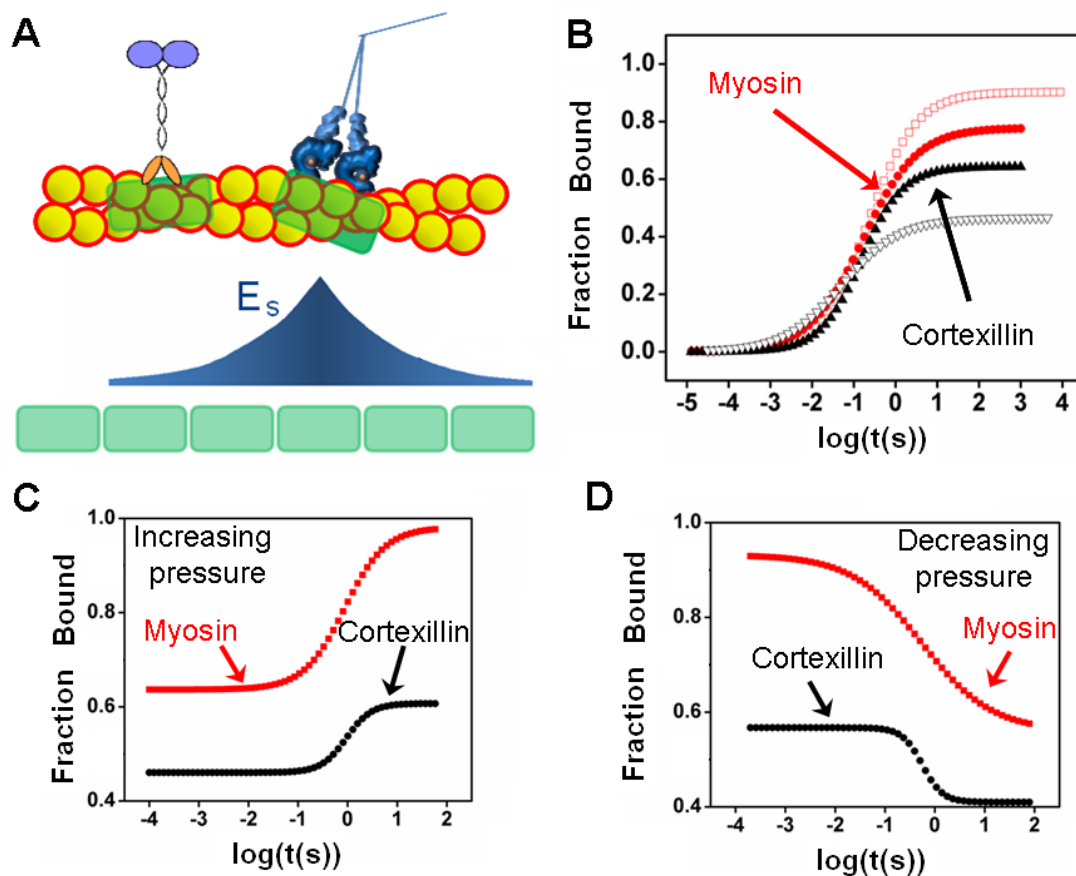
Figure S4. Kinetic Monte Carlo simulation of hetero-cooperative actin binding by myosin II and cortexillin I. (A) The strain field in the hetero-cooperative binding regime is shown. (B) Graph shows the binding curves of myosin alone (open red dots), cortexillin alone (open black triangles) and the mixture of myosin and cortexillin (the filled dots and filled triangles). (C) and (D) show the binding behaviors of the protein mixture in response to pressure jumps.
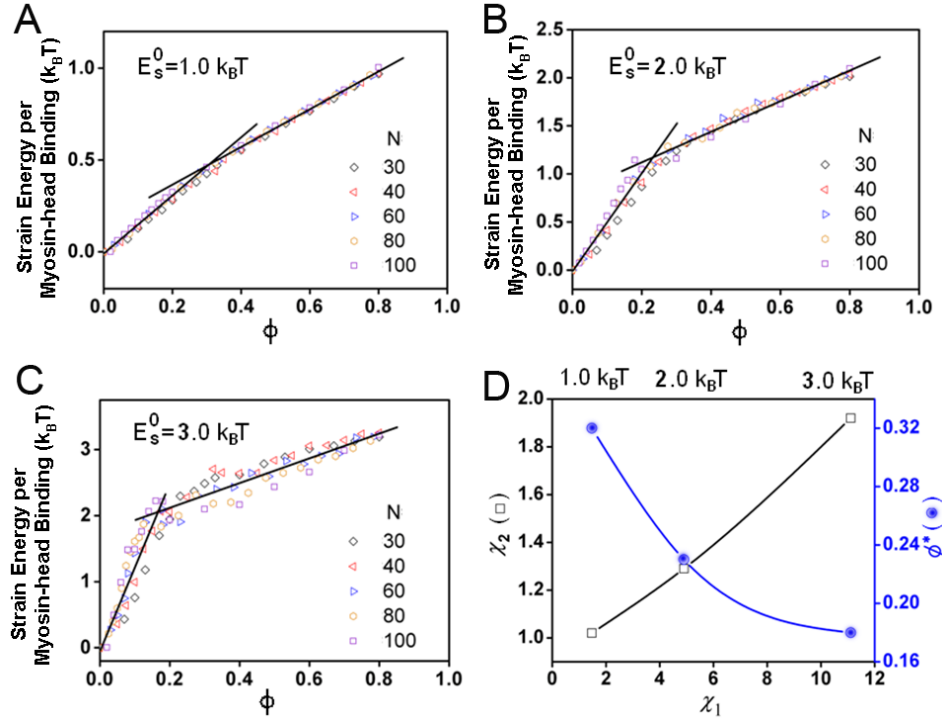
Figure S5. The mean-field approximation of strain energy per myosin-head binding. The change of binding energy is calculated from statistical mechanics for strain energy $E_s^{\;0}$ at 1 k_BT (A), 2 k_BT (B) and 3 k_BT (C) with different numbers of binding sites, N. Here, ϕ is the coverage of the actin filaments by the bound myosins. (D) The values of χ_1, χ_2 and ϕ^* at different strain energies ($E_s^{\;0}$ = 1, 2, 3 k_BT increasing from left to right).
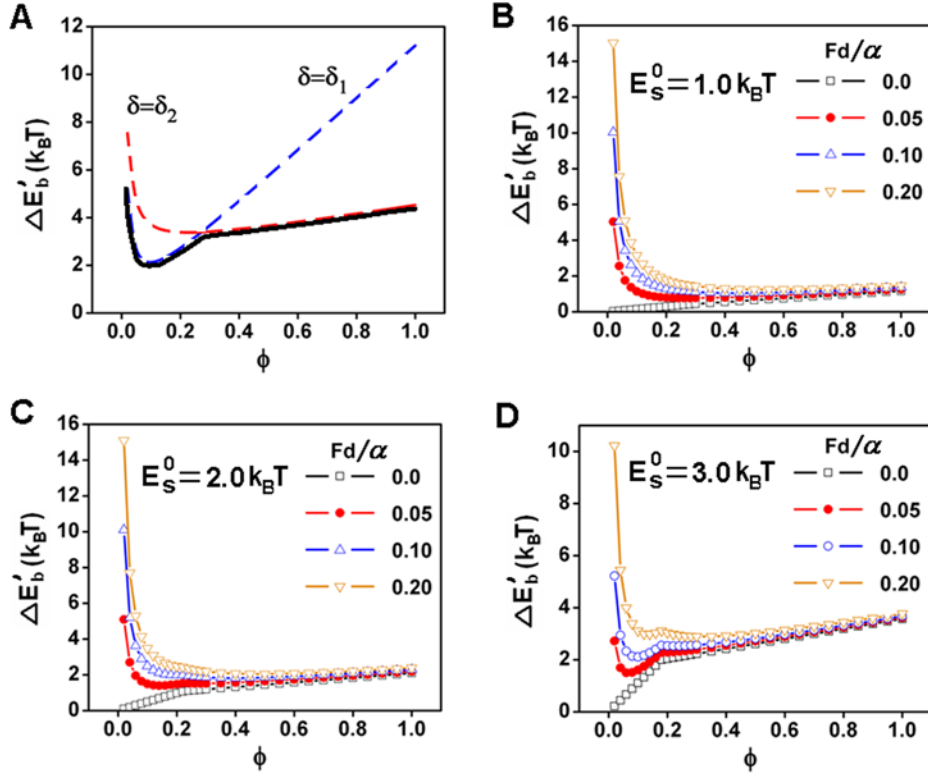
Figure S6. The dependence of $\Delta E_b'$ on m, the amount of bound myosin II. (A) A schematic plot shows how $\Delta E_b'$ (black solid line) changes its slope from δ_1 (blue dotted line) to δ_2 (red dotted line). The $\Delta E_b'$ changes as a function of m for different Fd/α when E_s^0 has a value of 1.0 $k_B T$ (B), 2.0 $k_B T$ (C) and 3.0 $k_B T$ (D).
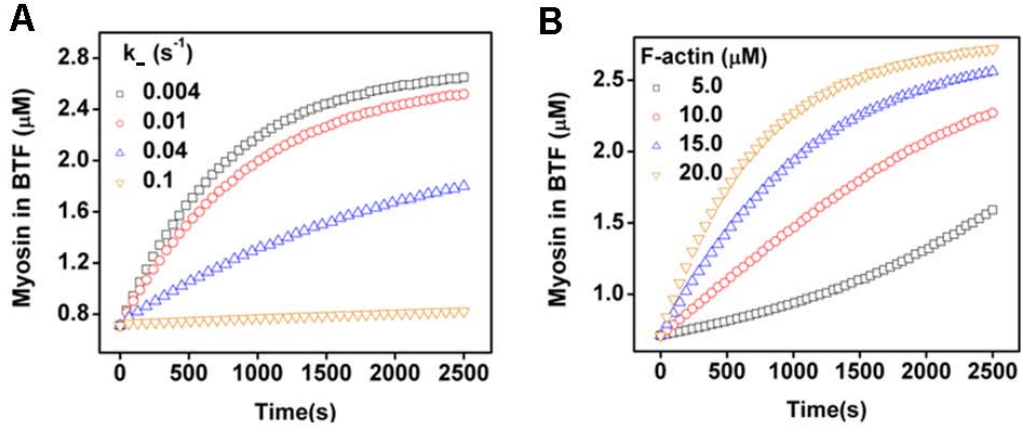
Figure S7. The kinetics of *in vitro* BTF assembly. (A) The assembly kinetics are shown for a fixed actin concentration but with different k_-. (B) The assembly kinetics are shown for different F-actin concentrations for $E_s^{\,0}$ at 1.0 $k_\mathrm{B}T$.
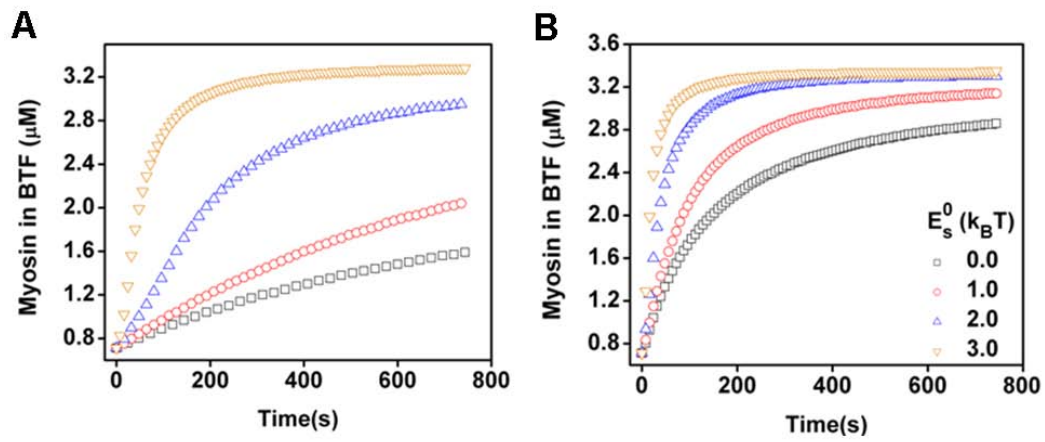
Figure S8. The myosin BTF assembly for k$_+$ at 6.6 s^{-1} (A) and 66.0 s^{-1} (B), respectively. For all cases $C_{myo\sin} = 3.4$ μM, $C_{actin} = 20.0$ μM, and $Fd = 0\ k_{B}T$.
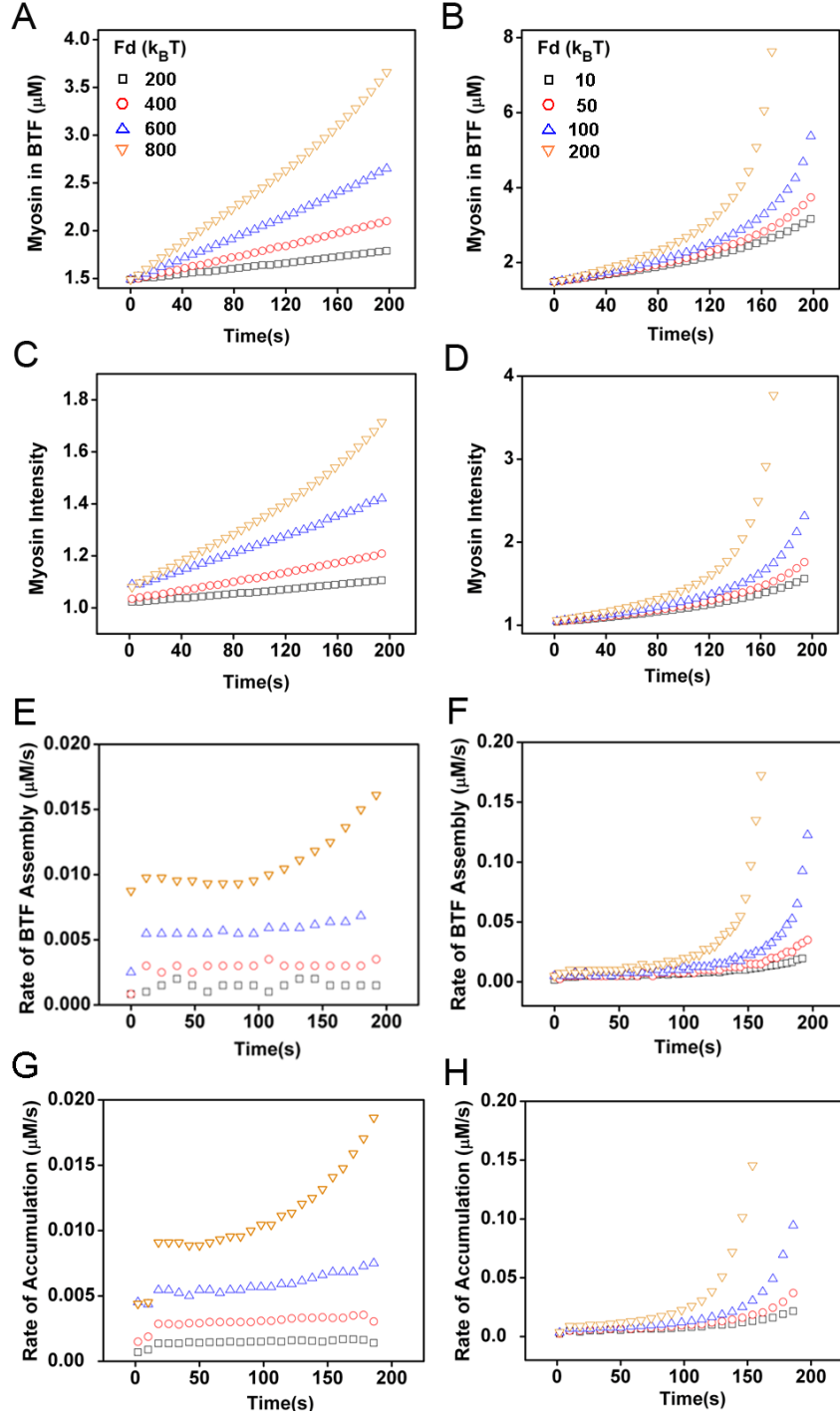
Figure S9. The BTF assembly, the associated myosin intensity and the corresponding rates are calculated at different Fd **values but with same cooperativity,** $E_s^0 = 3\ k_BT$**.** Left column is for k_1: 7 s^{-1} whereas right column is for k_1: 14 s^{-1}.
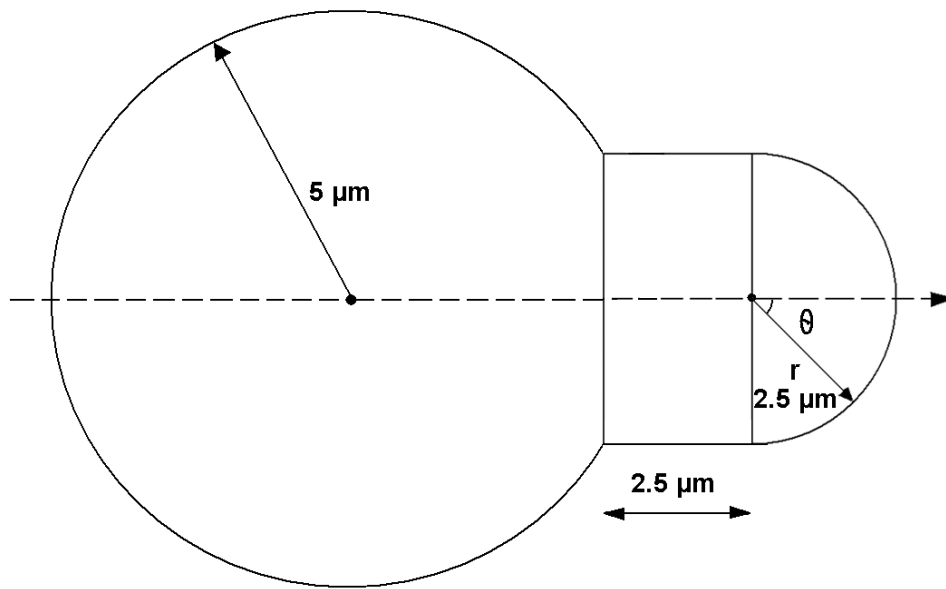
Figure S10. The geometry of the cross-section of the cell region aspirated into the micropipette used for 3D simulations in COMSOL.

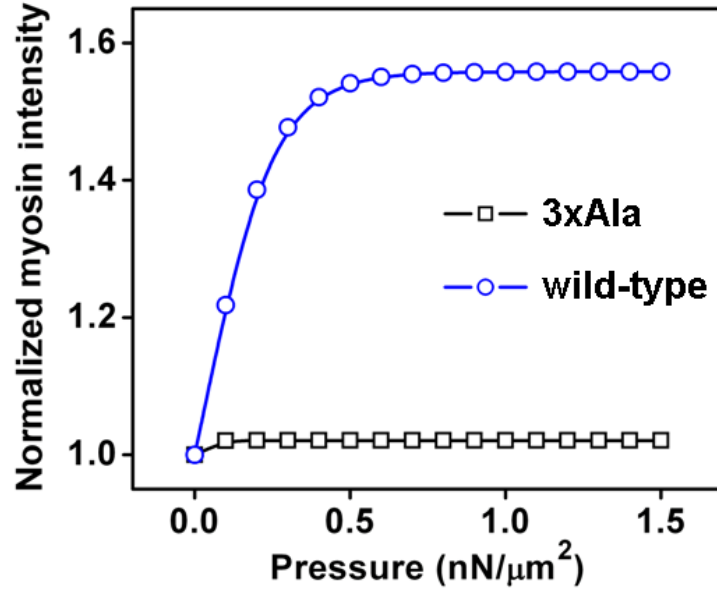**Figure S11. The normalized myosin intensity increased with the applied pressure, ΔP.** Here, the force-dependent term in Eq. 3, $Fd/\alpha m$, is rewritten as $\Delta P \Delta A d/(2\rho \Delta A h N_A m)$, where area $\Delta A = 1\,\mu m^2$, duty ratio $\rho = 0.06$, thickness of cell cortex $h = 0.5$ µm and N_A is the Avogadro's number.
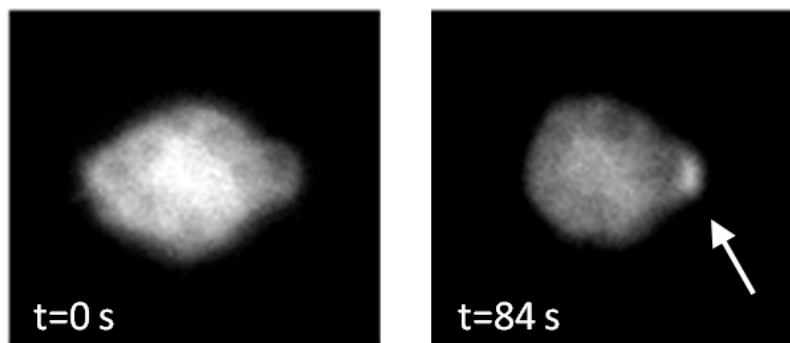
Figure S12. The accumulation of myosin heavy chain kinase C in response to pressure at different time frames.

Supplemental Movie Legends

Supplemental Movie 1. Movie shows the simulation result for cooperative binding of myosin II to actin filaments. The bound myosins (orange dots) form clusters on the actin filaments. The grey dots are the freely diffusing monomers. The time delays between each frame increase logarithmically.

Supplemental Movie 2. Movie shows the simulation result for cooperative binding of myosin II and cortexillin I. Clusters containing both myosin II and cortexillin I are formed due to hetero-cooperativity. The bound myosins and cortexillins are represented by yellow and red dots, respectively. The unbound myosins and cortexillins are represented by grey and green dots, respectively. The time delays between each frame increase logarithmically.

Supplemental Movie 3. Movie shows the accumulation of WT myosin II in response to applied force.

Supplemental Movie 4. Movie shows the accumulation of 3xAla myosin II in response to applied force.

Supplemental Movie 5. Movie shows a 3D view of WT myosin II accumulation in response to applied stress. The movie has an 85° cutout so that the cell interior is visible.